Development of novel genetically-encoded fluorescent probes to track ceramides during phagocytosis

Vladimir Girik[1], Larissa Van Ek[2,3], Isabelle Dentand Quadri[1], Maral Azam[1], Maria Cruz Cobo[1], Marion Mandavit[1], Isabelle Riezman[4], Howard Riezman[4], Anne-Claude Gavin[2,3], Paula Nunes-Hasler[1].

[1]Department of Pathology and Immunology, Geneva Center for Inflammation Research, Faculty of Medicine, University of Geneva, Geneva Switzerland

[2]Department of Cellular Physiology and Metabolism, Faculty of Medicine, University of Geneva, Geneva Switzerland

[3]Diabetes Center, Faculty of Medicine, University of Geneva, Geneva, Switzerland

[4]Department of Biochemistry, NCCR Chemical Biology, Faculty of Science, University of Geneva, Geneva Switzerland

***Corresponding Author:**

Paula Nunes-Hasler
Department of Pathology and Immunology
Geneva Center for Inflammation Research
Faculty of Medicine
University of Geneva,
1 Rue Michel-Servet
Geneva Switzerland 1211
Paula.Nunes@unige.ch

Key words: kinase suppressor of ras 1, SET nuclear proto-oncogene, I2PP2A, protein kinase c zeta, PRKCZ, C6-ceramide, sphingomyelinase, myriocin, fumonisin B1, stromal interaction molecule 1, Sec22b, lipidomics

Abstract

Ceramides (Cer) and their derivatives have been suggested to regulate phagocytosis, however their exact function remains poorly understood. Genetically-encoded fluorescent biosensors have been immensely useful in deciphering the critical role of phagosomal phosphoinositide regulation, and thus we sought to develop similar tools to examine Cer dynamics during phagocytosis. EGFP fusion of several known Cer-binding domains were generated and expressed in cells. While most constructs localized to the nucleus or cytosol, the CA3 cysteine-rich domain of the pseudokinase KSR1 displayed additionally plasma membrane (PM) or endolysosomal localization, depending on the position of the fluorescent tag and linker. C-terminally tagged KSR1-CA3 (C-KSR) and a more stable version C-KSR-GS responded as expected to Cer depletion and accumulation using a panel of Cer modifying drugs. In contrast, N-terminally tagged N-KSR did not respond to Cer induction by palmitate or glucosylceramide (GlcCer) synthase inhibitor Genz-123346. Liposome microarray analysis suggested N-KSR binding to the Cer derivative GlcCer. Interestingly, the three probes showed distinct dynamics during phagocytosis in model phagocytic fibroblasts. Despite partial lysosomal degradation, C-KSR robustly but transiently re-localized to the PM during phagocytosis, whereas N-KSR re-localized from the PM to the cytoplasm at later timepoints. Moreover, occasional weak recruitment of C-KSR-GS to endoplasmic reticulum and phagosome was enhanced upon overexpression of the endoplasmic reticulum proteins STIM1 and Sec22b, and was more salient in dendritic cells. The data suggest these novel probes may be valuable new members of the growing molecular toolkit used to analyze sphingolipid dynamics and function in living cells.

Introduction

Phagocytosis is a fundamental process whereby external foreign particles are internalized by cells, and the resulting membrane-engulfed compartment, called the phagosome, undergoes a series of maturation steps that lead to the formation of the digestive milieu and degradation of the foreign material (Levin, Grinstein, and Canton 2016). A large body of literature has highlighted the central role of dynamic phosphoinositide lipid remodeling in controlling this process through the recruitment of a variety of effectors including cytoskeletal, motor or vesicular docking proteins that help guide phagosomes to their fate (Levin, Grinstein, and Canton 2016; Yeung and Grinstein 2007; Levin, Grinstein, and Schlam 2015). Sphingolipids are a diverse group of lipids crucial for maintaining cellular membrane structure, fluidity, curvature, that have been long recognized to additionally play bioactive signaling roles (Quinville et al. 2021). Ceramides (Cer), a central hub of the sphingolipid network (Hannun and Obeid 2008; 2018), have also been implicated in various steps of the phagocytic process. These span from facilitation of receptor clustering and activation (Abdel Shakor, Kwiatkowska, and Sobota 2004; Avota, Gulbins, and Schneider-Schaulies 2011), to initial membrane deformation of phagocytic cups (Magenau et al. 2011; Niekamp et al. 2021), to promotion of phago-lysosome fusion (Schramm et al. 2008; Wu et al. 2018; Hinkovska-Galcheva et al. 2005), and inhibition of antigen presentation in dendritic cells (Sallusto et al. 1996; Eva Fuglsang, Louise Boye, and Hanne Frokiaer 2017). However, compared to phosphoinositides, less is known about the dynamics, regulation and roles of Cer and its related lipids during this critical immune process (Saharan, Mehendale, and Kamat 2022).

Arguably, part of the challenge may lie in the difficulty tracking these lipids in living cells (Canals, Salamone, and Hannun 2018). The most reliable methods such as mass spectrometry do not have the spatial resolution required for subcellular tracking (Buchberger et al. 2018), or rely on labor and material intensive organelle isolation that still suffer from contamination of sphingolipid-rich endoplasmic reticulum (ER) membranes due to tightly tethered membrane contact sites (MCS) (Scorrano et al. 2019). In addition, tools such as fluorescent sphingolipid analogs are rapidly metabolized and may partition in membranes differentially (Canals, Salamone, and Hannun 2018). Moreover, permeabilization steps necessary for allowing access of anti-Cer antibodies to intracellular membranes such as phagosomes may also disrupt natural lipid localization (Bjørnestad and Lund 2023). Therefore, an approach enabling detection of Cer in living cells with high spatial resolution is desirable. Genetically encoded lipid probes, typically composed lipid-binding domains coupled to a fluorescent tag, provide an opportunity to investigate subcellular localization, relative accessibility, and dynamics in living cells, and have been extensively employed to dissect phospholipid dynamics during phagocytosis (Hammond et al. 2022). Few described lipid

90 probes specific for sphingolipids have been published (Yamaji et al. 1998; Bakrač et al. 2010).
91 Moreover no fluorescent Cer biosensor based on isolated Cer-binding domains have been
92 described so far, although a range of full-length Cer-binding proteins have been employed
93 (Bidlingmaier et al. 2016; Bockelmann et al. 2018; Deng et al. 2021; K. Zhou et al. 2018)., and
94 a GST-fusion of the Cer binding domain of the pseudokinase KSR1 has been used *in vitro*
95 (Yin et al. 2009). In the current report, we document the development and characterization of
96 novel putative Cer-binding genetically encoded fluorescent probes. Out of several potential
97 Cer-binding biosensors, the cysteine-rich domain of the human pseudokinase KSR1 (Yin et
98 al. 2009) was the most promising candidate. KSR1-based probes responded robustly to
99 treatments modifying Cer levels in cells, though differences were noted between C- terminally
100 N-terminally tagged constructs, and probe instability appeared to contribute to this response.
101 Although weak *in vitro* binding precluded in-depth biochemical characterization, liposome
102 microarray data indicate that N-KSR constructs may instead be sensitive to glycosylated Cer.
103 Interestingly, differential probe localization depending on cell type and expression of ER-
104 localized constructs were documented to occur during phagocytosis in model phagocytes.
105 Together our data indicate that these constructs may be useful tools for dissecting subcellular
106 sphingolipid dynamics and warrant further characterization.

107

108 **Results**

109 **KSR1-based probes show membrane-associated localization**

110 To identify ceramide-specific biosensors, four domains that have been previously
111 demonstrated to bind ceramides *in vitro* and/or *in vivo* were selected: 1) the earmuff domain
112 (EMD) of the human SET protein [amino acids (aa) 70-226] (Mukhopadhyay et al. 2009); 2)
113 the N-terminal fragment of atypical human protein kinase C zeta (PRKCZ, also called PKCζ)
114 containing a lipid-binding C1 domain (aa 123-193); 3) the C20-kD carboxy-terminal domain
115 (amino acids 405-646) of PRKCZ (Wang et al. 2005; 2009); and 4) the C1 cysteine-rich
116 domain (CA3, also called CRD, amino acids 317-400) of the human pseudokinase KSR1 (Yin
117 et al. 2009) (Fig 1A). The selected domains were tagged with EGFP at the N- or C-terminus
118 (prefixed with N- and C- respectively) and expressed in mouse embryonic fibroblasts (MEFs).
119 All SET and PRKCZ-based fusion proteins were primarily localized to the nucleus (Fig 1B-C).
120 A nuclear export signal (NES) was added to C-PRKCZ-C20 and C-SET-EMD chimeras to
121 release proteins trapped in the nucleus, a strategy previously used for lipid biosensor
122 construction (Goulden et al. 2019). C-NES-PRKCZ-C20 and C-NES-SET-EMD were mainly
123 found in the cytosol, though nuclear localization was still noticeable (Fig 1B-C). In contrast,
124 the expression pattern of KSR1-based constructs depended on the position of the fluorescent

125 tag. N-KSR1(317-400) (abbreviated N-KSR) was found primarily at the plasma membrane
126 (PM), while the C-terminally tagged probe (C-KSR) localized to intracellular vesicles some of
127 which appeared enlarged (Fig 1D). The localization of both N- and C-KSR constructs was
128 dependent on two conserved cysteines in the C1 domain (C359/C362) whose mutation to
129 serine was shown previously to decrease ceramide binding *in vitro* (Yin et al. 2009) (Fig 1D).
130 To potentially increase the affinity for ceramides, a construct expressing two KSR1 CRDs in
131 tandem fused at the C-terminus to EGFP was also created (abbreviated 2X-C-KSR), following
132 another strategy previously used for lipid biosensor construction (Hammond et al. 2022).
133 However, the localization appeared similar to that of N-KSR. When expressed in human Hela
134 cells, KSR1-, SET-, and PRKCZ-based displayed an expression pattern similar to that of MEFs
135 (Fig S1). In previous studies, anti-ceramide antibodies primarily stained the plasma membrane
136 and the Golgi (Krishnamurthy, Dasgupta, and Bieberich 2007; Wang et al. 2009) whereas
137 exogenously added azido-functionalized ceramides partitioned into the PM and organellar
138 membranes, including mitochondria and lysosomes (Walter et al. 2017; Götz et al. 2020). Of
139 all candidate probes tested, only KSR1-based constructs showed salient membrane-
140 associated staining and were therefore selected for further validation.

141

142 **KSR probes respond to the changes in ceramide levels**

143 Next, the behavior of KSR probes in response to ceramide depletion or accumulation was
144 investigated. To induce ceramide depletion, cells were exposed to well-known inhibitors of
145 sphingolipid biosynthesis: myriocin (Myr), a potent inhibitor of serine-palmitoyltransferase
146 (SPT) (Miyake et al. 1995), the enzyme which catalyzes the first step in SL biosynthesis; and
147 fumonisin B1 (FumB1), a selective inhibitor of ceramide synthases (Merrill et al. 2001).
148 Transfected MEF cells showed significant variation in the expression of KSR probes from one
149 cell to another, making it challenging to assess the effect of SL inhibitors on probe localization
150 and abundance. To circumvent this issue, the KSR probes were re-cloned into Sleeping
151 Beauty transposon vectors (Ivics et al. 2009) and co-transfected with the transposase to
152 generate MEF stable cell lines. Surprisingly, C-KSR-expressing cells demonstrated a drastic
153 5-fold decrease in the intracellular fluorescence after a 3-day incubation with Myr (0.5 μM) or
154 FumB1 (2.5 μM), accompanied by some re-localization to the cytosol in a subset of cells (Fig
155 2A-B). In comparison, only a 2.5-fold decrease in the probe intensity was observed in N-KSR1
156 expressing cells after sphingolipid depletion with either drug (Fig 2C-D). As expected, all major
157 sphingolipids including ceramides (Cer), glycosylated ceramides (including glucosyl and
158 galactosyl ceramides, collectively termed hexosyl-ceramides, HexCer) and sphingomyelins
159 (SM), were markedly depleted by Myr treatment as measured by targeted quantitative tandem

160 mass-spectrometry lipidomic analysis (Fig 2E, Supplementary Data S1) (Guri et al. 2017). In
161 addition, Myr treatment of MEF cells transiently transfected with C-KSR and cytosolic TagRFP
162 did not produce any noticeable effect on TagRFP expression (Fig S2), confirming a specific
163 effect on KSR constructs.

164 To induce Cer accumulation two methods were employed: treatment with the Cer precursor
165 C16 acyl-chain fatty acid palmitate (Tran et al. 2016; Kiefer et al. 2015) or incubation of purified
166 bacterial sphingomyelinase from *Staphylococcus aureus* (SMase), which releases ceramides
167 by hydrolyzing sphingomyelin on the outer leaflet of the PM (Devaux 1991; Abe and Kobayashi
168 2014), where ceramides are believed to partition efficiently in both leaflets in eukaryotic cells
169 (Pohl et al. 2009). After a 4h incubation in palmitate complexed to BSA (Palm) a 2.7-fold
170 increase in C-KSR signal intensity was observed compared to cells treated with delipidated
171 BSA alone (Fig 2A-B). However, the N-KSR fluorescence intensity was unchanged, and no
172 obvious changes in localization were observed (Fig2C-D). Lipidomic analysis confirmed that
173 Palm induced a 2-fold accumulation of Cer species, driven mainly by the 4-fold increase in
174 C16-Cer (Fig 2F, Supplementary Data S1). However, unexpectedly depletion of C24-SM
175 ($p<0.001$), and C24-HexCer ($p=0.0144$) was also observed (Fig 2F, Supplementary Data S1).

176 We then treated C-KSR expressing cells with SMase (0.5 U/ml) for 30 min. This led to C-KSR
177 recruitment to the PM (Fig 3A-C), where both the fluorescence intensity at the PM, the total
178 cellular fluorescence or blinded quantification of the fraction of cells displaying PM localization
179 were higher in SMase treated cells compared to PBS-treated controls ($p=0.0004$, $p=0.0007$
180 and $p= 0.0001$ respectively, Fig 3B-C). Lipidomic analysis confirmed that SMase induced a
181 dramatic 40-fold accumulation of Cer species, driven by C16-Cer ($p<0.0001$) (Fig 3D,
182 Supplementary Data S1). Total HexCer were not different but increases in C10-HexCer
183 ($p=0.0406$), a lipid of unknown biological significance, were observed (Fig 3D, Supplementary
184 Data S1). Although total SM was not significantly different, reductions in longer chain C20-
185 C22- and C24-SM were observed ($p=0.0052$, $p=0.0117$, $p= 0.0052$, respectively, Fig 3D,
186 Supplementary Data S1). That cleavage of sphingomyelin was efficient was also confirmed
187 by staining with a purified EGFP-tagged SM-specific probe lysenin (Kwiatkowska et al. 2007)
188 (20 μg/ml) Fig S3A). Since SMase treatment triggered the largest Cer accumulation, as well
189 as salient PM recruitment and global increase in fluorescence with the C-KSR probe, C-NES-
190 PRKCZ-C20 and C-NES-SET-EMD were also examined under conditions of SMase
191 treatment. However, no changes in localization or overall fluorescence were noted (Fig S3B).
192 In addition, since diacylglycerol (DAG) is a molecule with close structural similarity to ceramide
193 that could potentially be generated by activation of SM synthases upon large increases of Cer
194 (Goñi and Alonso 1999; Ekman et al. 2015), the specificity of the C-KSR for ceramide was

195 further investigated by co-expression C-KSR-mRFP with the DAG probe GFP-PKC-C1(2)
196 from the tandem C1 domains of the rat PKCγ (Codazzi, Teruel, and Meyer 2001). Cells were
197 then treated with either 10 μM ionomycin (Iono) for 10 min, reported to induce PM DAG
198 accumulation (Botelho et al. 2000) or with SMase as above. Whereas Iono treatment but not
199 SMase induced PKC-C1(2) PM recruitment ($p<0.0001$ Iono, $p=0.5214$ SMase), the opposite
200 pattern was observed for C-KSR ($p=0.1854$ Iono, $p=0.0065$ SMase, Fig 3E-F). Co-expression
201 of the two probes could not explain these observations as treatment with SMase did not affect
202 the localization of PKC-C1(2) when expressed alone, nor did it affect the localization of an
203 alternate DAG probe YFP-DBD (C1b DAG-binding domain of PKCß) (Gallegos, Kunkel, and
204 Newton 2006) (Fig S3C), ruling out potential DAG generation by SMases (Ekman et al. 2015).
205 Collectively, the data suggest that C-KSR is sensitive to the changes in cellular levels of Cer
206 and can detect locally generated ceramides at the PM.

207

208 **C-KSR is degraded in lysosomes**

209 *De novo* biosynthesis of Cer occurs in the ER, after which Cer are shipped to the Golgi for
210 conversion into SM and complex sphingolipids. However, Cer can also be generated at the
211 PM, in endolysosomal compartments, or mitochondria via hydrolysis of HexCer or SM
212 (Hannun and Obeid 2018). Thus, to determine whether C-KSR might sense different
213 subcellular pools of Cer we next sought to define in greater detail the organellar distribution of
214 C-KSR. Immunostaining against various organelle markers revealed that C-KSR colocalized
215 preferentially with late endosome Rab7 and lysosome markers LAMP1, but not with recycling
216 endosome-resident Transferrin (Tfn), nor with early endosomal marker Rab5, or Golgi marker
217 TGN38 (Fig 4A-B, Fig S4). Despite the fact that C-KSR appeared to reside on the membrane
218 of enlarged vesicles (for example Fig 1D inset), a closer examination of the LAMP1 staining
219 indicated that LAMP1 was still often peripheral to C-KSR, even in vesicular structures with a
220 dark lumen (Fig 4A, bottom inset arrow). Such structures were reminiscent of autolysosomes,
221 pointing to C-KSR transport into the degradative compartments. Immunoblots of lysates from
222 MEFs stably expressing the KSR probes corroborated this hypothesis, showing extensive
223 degradation of C-KSR1, while protein cleavage was much less evident for N-KSR1 (Fig 4C).
224 Thus, if C-KSR is stabilized or protected from degradation upon membrane binding,
225 pronounced degradation of C-KSR may explain the increase and decrease in global C-KSR
226 fluorescence intensity after treatment with ceramide inducing or depleting drugs. Moreover,
227 C-KSR degradation accounts for the observed colocalization with the late endosomes and
228 lysosomes, though C-KSR was also present in the cytosol and at low levels at the PM in a
229 subset of cells.

230

231 **Differential response of N- and an improved C-KSR probe**

232 The extensive degradation of C-KSR probe, but not N-KSR, prompted us to scrutinize the
233 sequences of the constructs. The main difference was the short linker regions between the
234 lipid-binding domains and the fluorescent tag. N-KSR contained flexible linkers rich in small or
235 polar amino acids such as glycine and serine (GS linkers), which are widely used for
236 constructing multidomain chimeric proteins (Chen, Zaro, and Shen 2013). For the construction
237 of the C-KSR probe, the lipid-binding domain was subcloned into restriction sites of the
238 pEGFP-N1 backbone, which inadvertently introduced an RLELKLRILQ amino acid motif that
239 targets cytosolic proteins for lysosomal degradation via chaperone-mediated autophagy
240 (CMA) (Majeski and Fred Dice 2004). To render the C-KSR probe more stable, the old linker
241 was replaced with the short flexible GS sequence (GGSSGGGGA), as in the N-KSR (Fig 4D).
242 The resulting chimeric probe was renamed C-KSR-GS. When transiently expressed in MEFs,
243 C-KSR-GS was much less prone to degradation, as demonstrated in the representative
244 immunoblot (Fig 4E). The subcellular localization of the novel C-KSR-GS-EGFP fusion was
245 then examined by confocal microscopy. Images revealed localization to the PM and the
246 cytosol, similar to the expression pattern of the N-KSR and the tandem KSR probes (Fig. 5A-
247 C, compared to Fig 1D). Cells transfected with C-KSR-GS were then exposed to Cer depleting
248 FumB1, or Cer inducing Palm and SMase to determine the response of this new probe to Cer
249 modulation. Similar to the other probes, a reduction in global fluorescence upon treatment with
250 FumB1 (Fig 5A, p=0.039) was observed. Interestingly an increase in global fluorescence upon
251 incubation with Palm, observed with C-KSR but not N-KSR was discerned, though the fold
252 difference was smaller (2.7-fold increase for C-KSR see Fig 2B, and 1.5-fold increase for C-
253 KSR-GS, p=0.048, Fig 5B). Moreover, after treatment with the bacterial SMase, the fraction
254 of cells displaying PM localization increased from approximately 35 to 54% (p<0.0001)
255 indicating that C-KSR1-GS, like C-KSR also responds to ceramide upregulation at the PM (Fig
256 5C). To further explore potential differences in response to Cer modulation between N-KSR
257 and C-KSR-GS we compared the response of the two probes to reagents previously shown
258 to increase cellular ceramides. To this end cells expressing either probe were treated for 2h
259 with 200 μM Cer analogue C6 (d18:1/6:0) (Kjellberg et al. 2015) or overnight with 200 μM of
260 the GlcCer synthase inhibitor Genz-123346 (Genz) (H. Zhao et al. 2007) or their respective
261 vehicle controls. Interestingly, whereas both probes showed a robust increase in cellular
262 fluorescence upon treatment with C6 (p=0.011 for C-KSR-GS, p=0.0031 for N-KSR, Fig 5D-
263 E) as compared to vehicle, they again displayed a striking differential response to Genz
264 treatment, where an increase in fluorescence was observed wtih C-KSR-GS (p=0.0413) but
265 not with N-KSR (p=0.3526) (Fig 5D-E). Together these data suggest that all 3 KSR-based

266 probes may have an inherent instability that is mitigated upon membrane binding, which
267 explains the global fluorescent response to Cer modifying drugs, but that N- and C-terminal
268 tagging may nevertheless affect the nature of the lipid (or lipids) bound.

269

270 **Analysis of lipid binding by KSR probes**

271 In light of the intriguing differences in localization and responses to Palm and Genz treatments,
272 we next sought to further characterize the lipid-binding profile of N- and C-KSR-based probes.
273 To this end we employed a high-throughput liposome microarray (LiMa) technology, where
274 arrays of liposomes (small artificial vesicles) of various compositions are deposited inside a
275 microfluidic chip, exposed to purified proteins or cell lysates, and binding is assessed by
276 automated microscopy (Saliba et al. 2014). To obtain purified probes, the N-KSR and C-KSR
277 probes were re-cloned into super-folding GFP (sfGFP) bacterial expression vectors (Pédelacq
278 et al. 2006) and purified from *E.coli* cultures, where N-KSR was easily obtained but C-KSR
279 had a tendency to aggregate, though smaller soluble quantities were still obtained. DOPC
280 (dioleoyl-phosphatidylcholine), with fluorescent 0.1% phosphatidylethanolamine (PE)-Atto647
281 and 0.5% PE-PEG350 stabilizer (Magic lipid) served as a backbone for liposomes containing
282 2, 5 or 10% bovine Cer mixture (CER), chicken SM mixture (SM), C17-glucosyl(β)-ceramide
283 (d18:1/17:0, GlcCer), Sphingosine (d18:1, Sph), Ceramide-1-Phosphate (16:0, C1P) or DO-
284 PI(4,5)P2 (dioleoyl-phosphatidylionositol-(4,5)-bisphosphate). It should be noted that Cer and
285 Sph have been previously reported to destabilize membranes or form aggregates (Veiga et
286 al. 1999; Montes et al. 2002; Contreras et al. 2006) and in general, in our hands, liposome
287 spots containing sphingolipids were prone to aggregation, deformation or wash-out, rendering
288 many spots unusable. However, when small zones of characteristic spherical liposome
289 structure where obtained, these were analyzed, with the caveat that lipid partitioning or
290 segregation cannot be excluded. Nevertheless, observations were possible with all liposome
291 compositions except for mixtures containing 5 and 10% GlcCer, where liposomes where never
292 obtained. Overall, out of 5 chips containing 20 arrays, 3 arrays with purified N-KSR (missing
293 2 spots) and 2 arrays (missing 6 spots) with purified C-KSR were successfully analyzed (Fig
294 6A-B, Supplementary Data S2). Considering statistical analysis for liposomes represented in
295 at least 3 spots, low but significant normalized binding intensity (NBI) scores were observed
296 between N-KSR and liposomes containing 2% GlcCer as compared to DOPC liposomes
297 (p=0.0018). Although sample size was too low for a meaningful statistical analysis,
298 morphological examination of images also suggested a potential weaker binding of N-KSR to
299 C1P and of C-KSR probe to liposomes with 10% CER (Fig 6B).

300 Although we were not able to obtain purified C-KSR-GS, we next performed LiMa analysis
301 using lysates from transfected HEK293 cells. Since the *in vitro* binding of the probes was
302 weak, the use of lysates might also provide missing auxiliary components such as co-factors
303 and proteins to improve binding affinity. In addition, Since purified N-KSR did not appear to
304 bind liposomes containing bovine CER mixtures, the liposome composition of the arrays was
305 modified to include a broader variety of ceramides as well as additional lipids including: the
306 intermediate fatty acid chain-length ceramide C18-ceramide (d18:1/18:0, C18CER); the
307 ceramide precursor dihydroceramide (d18:0/d18:0, C18DHCER) which harbors an identical
308 headgroup as ceramide; sphingosine-1-phosphate (d18:1, S1P); DAG (d18:1/18:1); as well
309 as DO-phosphatidic acid (DOPA), though the latter was found to auto-fluoresce, and so was
310 excluded from the analysis. Liposomes containing 10-15% DAG producing large brightly
311 fluorescent aggregates were also excluded. C-KSR lysates were not included since the
312 fraction of intact probe as compared to released EGFP was small (see Fig 4C). However, in
313 6 chips with 3 arrays for each probe (missing 12 spots out of 78 for both N-KSR and C-KSR-
314 GS), neither N-KSR nor C-KSR-GS showed signs of binding to any of these liposome
315 compositions (Fig S5A-B, Supplementary Data S2). Since in intact cells C-KSR-GS binds the
316 PM and might require a more complex lipid combination for successful binding, we then we
317 sought to mimic the composition of the inner plasma membrane (IPM) leaflet (Lorent et al.
318 2020). To this end, IPM liposome backbones were prepared using: 30.2% palmitoyloleoyl-
319 phosphatidylcholine (POPC); 15% PO-phosphatidylethanolamine (POPE); 33% cholesterol;
320 21.2% DO-phosphatidylserine (DOPS); and 2,5, or 10% of the bovine CER mixture (CerMix),
321 C18DHCER, C18CER, DAG, chicken SM mixture (SM) and Sph. Next, the binding profile of
322 the C-KSR1-GS probe was examined and compared to lysates of soluble EGFP as a negative
323 control and PKC-C1(2) as positive control. In total out of 4 chips, 3 arrays for C-KSR-GS
324 (missing 14 out of 78 spots), 3 arrays of EGFP (missing 7 out of 78 spots) and 3 arrays of
325 PKC-C1(2) (missing 6 out of 78 spots) were successfully quantified. Using the automated
326 quantification pipeline, whereas robust and significant binding of PKC-C1(2) to DAG-
327 containing liposomes as compared to IPM liposomes was readily observed ($p<0.0001$ for both
328 2% and 5% DAG, Fig S5C-D, Supplementary Data S2), there were no significant differences
329 in NBI scores of C-KSR-GS liposome binding as compared to liposomes of IPM composition
330 alone (Fig 6C, Supplementary Data S2). However, a closer examination of the images
331 revealed striking morphological differences between C-KSR-GS and EGFP (Fig 6D, Fig S5E).
332 Whereas EGFP was often found encapsulated into liposomes regardless of composition, with
333 no signs of external binding, C-KSR-GS was only rarely found encapsulated, and instead the
334 images suggested a potential weak binding, particularly to Cer containing liposomes, though
335 faint binding was also discernible for DAG and IPM alone (Fig 6D, Fig S5E). Although it difficult
336 to draw definitive conclusions from these *in vitro* screens, which do not fully recapitulate

337 conditions in cells, together the data hint at a difference in the binding profiles of the KSR1-
338 based probes that could explain the difference in their response to Cer induction by Palm and
339 Genz (Fig 2B vs 2D, Fig 5D vs 5E). Thus, C-KSR and C-KSR-GS may require a more complex
340 membrane context or other co-factors in order to bind Cer species with higher affinity. On the
341 other hand, the data suggest that N-KSR might instead be sensitive to GlcCer which are
342 decreased upon treatment with both Palm and Genz at the same time that Cer is increased
343 (Fig 2F), which could result in no net change if some affinity for Cer exists.

344

345 **Behavior of KSR probes during phagocytosis**

346 In several reports, Cer generation has been associated with phagocytic ingestion and
347 phagosomal maturation, and shown to be important for pathogen elimination, yet its precise
348 role is still poorly understood (Pathak et al. 2018; Tafesse et al. 2015). Thus, to not only glean
349 some hints at Cer dynamics (and eventually function) during this important immune process,
350 but also to test our probes under a physiological stimulus, we next investigated the behavior
351 of our three KSR probes during phagocytosis. To this end, we examined MEFs rendered
352 phagocytic by overexpression of the FCGR2A-c-myc, a phagocytic cell model that are easier
353 to transfect and manipulate than naturally phagocytic cells, and which we and others have
354 observed to recapitulate many aspects of the phagocytic process, including phospholipids
355 dynamics (Giodini, Rahner, and Cresswell 2009; Bodman-Smith et al. 2004; Hinkovska-
356 Galcheva et al. 2005; Santos et al. 2022). Cells expressing each of the 3 KSR probes (N-, C-
357 and C-KSR-GS) were exposed to 3 µm IgG-opsonized polystyrene beads for 30 min or 135
358 min, time-points representative of early and late stages of phagosomal maturation (Fig 7A-C).
359 In parallel, sphingolipids levels were measured in C-KSR-expressing cells using targeted
360 lipidomics as described above, where a large accumulation in total cellular Cer, SM and
361 HexCer (4-, 2.6- and 6-fold, p=0.0002, 0.0204 and 0.0349, respectively) was observed at 30
362 min (Fig 7D, Supplementary Data S1). This effect was driven by changes in C24-Cer -SM and
363 -HexCer species as well as C16-Cer and -HexCer (Fig 7Di-iii, Supplementary Data S1). It
364 should be noted that large changes in total PC, PI and PS phospholipids were also observed
365 (Fig S6A), which grossly biased the usual normalization procedure. Thus, rather than
366 normalizing each individual sample by its own total glycerophospholipids, individual samples
367 were first normalized by their corresponding total protein, and the entire dataset was
368 normalized by the average daily total glycerophospholipid levels to obtain mol% values.

369 Interestingly, 30 min after the incubation with the IgG-coupled beads, accumulation of C-KSR
370 could be observed at the PM, similar to what was observed after incubation with bacterial
371 SMase (Fig 7A, see also Fig 3A). Exploring this PM localization further, we found PM staining

372 of C-KSR could still be detected at 45 min and 60 min after phagocytosis initiation, yet was
373 lost at later stages, after 90 and 135 min (Fig S6B). Similarly, PM localization of N-KSR and
374 C-KSR-GS was salient at 30 min (Fig 7B-C), even though both constructs were already found
375 at the PM under basal conditions, whereas at 135 min the N-KSR PM signal was not as clearly
376 discerned (Fig 7B). Moreover, whereas N-KSR was completely absent from phagosomes (Fig
377 7B, insets), in C-KSR-GS-expressing cells, accumulation around phagosomes was discerned
378 in a subset of phagosomes (Fig 7C, arrows). In some instances, a pattern of small flattened
379 cisternae or protruding tubular structures could be seen around phagosomes, which were
380 reminiscent of membrane contact sites (MCS) between the phagosomal membrane and ER,
381 structures that have been studied extensively by our laboratory in the past (Guido, Demaurex,
382 and Nunes 2015; Nunes et al. 2012; Nunes-Hasler et al. 2017; Santos et al. 2022) (Fig 7C,
383 arrows). To confirm whether such structures could indeed represent ER, C-KSR-GS was then
384 co-expressed with several ER-targeted constructs, including: a soluble ER-targeted RFP
385 TagRFP-KDEL, a calcium regulator and MCS marker mCh-STIM1 and mCh-Sec22b, an ER-
386 ERGIC protein that we have recently shown to be present in STIM1-independent MCS (Nunes
387 et al. 2012; Santos et al. 2022) (Figs 7E-F, Fig S6E). Interestingly, though overlap between
388 C-KSR-GS and KDEL was not easily discerned, likely due to low overall KDEL expression
389 (Fig S6E), overlap with STIM1 and Sec22b was observed in some but not all instances of
390 periphagosomal accumulation of the fluorescent proteins (Fig 7E-F). Finally, we expressed
391 the N-KSR and C-KSR-GS probes in a naturally phagocytic dendritic cell JAWS II. Similar to
392 MEFs, N-KSR did not localize to the phagosomal or other organellar membranes and
393 appeared to be depleted from the PM at late phagocytic time points (Fig 8A). In contrast,
394 robust C-KSR-GS accumulation at the phagosomal membrane could be discerned on a subset
395 of phagosomes, as well as on internal structures reminiscent of the ER (Fig 8B). Together
396 these intriguing observations suggest the following: first, that the large changes in Cer during
397 the first 30 min of phagocytosis detected in whole-cell MEF extracts are likely occurring at the
398 PM and are best detected by C-KSR which is the most sensitive of the 3 probes at detecting
399 changes of PM Cer. Second, that C-KSR-GS may more be useful to detect Cer species on
400 intracellular membranes including phagosomal and ER membranes. Finally the data also hint
401 at dynamic Cer fluxes, potentially between phagosomal membrane and ER at MCS.

402

403 **Discussion**

404 Despite a large number of proteins reported as Cer binders (Canals, Salamone, and
405 Hannun 2018; Bockelmann et al. 2018; K. Zhou et al. 2018), to our knowledge no genetically
406 encoded Cer-specific probe per se have not been reported, though whole GFP-tagged Cer-

407 binding proteins have been employed to track subcellular Cer in a limited number of studies
408 (Canals, Salamone, and Hannun 2018). Out of 14 candidate biosensor constructs reported
409 here, we focused on 3 based on the KSR1(317-400) Cer-binding domain which displayed
410 morphology of membrane localization. In contrast, constructs based on PRKCZ and SET were
411 either targeted to the nucleus, or, for those bearing a nuclear export signal (NES), did not
412 respond to SMase treatment (Fig S3). Since sphingomyelinases and ceramidases have been
413 reported in the nucleus, and indeed SET has a defined nuclear activity (Adachi, Pavlakis, and
414 Copeland 1994), it is possible that these proteins may detect nuclear Cer rather simply being
415 misfolded (Albi and Viola Magni 1997; Shiraishi, Imai, and Uda 2003), although the diffuse
416 rather than nuclear membrane localization is unexpected. Future studies employing stimuli
417 known to induce nuclear Cer may still help to verify the utility of these constructs.

418 In contrast, though nuclear shuttling has also been reported for KSR1, this scaffolding
419 regulator MAPK signaling normally resides in the cytosol in resting conditions (Brennan et al.
420 2002). It is recruited to the PM upon growth factor stimulation, which induces both changes
421 in the phosphorylation status of multiple KSR1 sites, as well as inducing the activities of neutral
422 and acidic SMases, generating Cer (Mathias, Peña, and Kolesnick 1998; Razidlo et al. 2004).
423 Thus KSR1-based probes are particularly poised to detect Cer in the context of PM lipids, and
424 the baseline localization of N-KSR, 2x-C-KSR as well as C-KSR-GS, as well as recruitment to
425 PM upon SMase treatment of C-KSR and C-KSR-GS are all consistent with this notion. In
426 addition to Cer binding, mutagenesis studies suggest that phosphorylation of T274 and S392
427 contribute to KSR1 stability, and in particular dephosphorylation of S392, the latter part of the
428 CA3 domain, participates in membrane re-localization upon growth factor activation (Brennan
429 et al. 2002; Razidlo et al. 2004). Whether S392 in the CA3 of our KSR constructs is
430 constitutively dephosphorylated, or whether separation from other KSR1 domains is sufficient
431 to allow conformational changes favoring Cer binding remains to be defined, though full-length
432 KSR1-S392A localizes to the nucleus rather than PM (Brennan et al. 2002). Several studies
433 have reported direct Cer binding, including *in vitro* studies using an N-terminal GST-fusion
434 with a CA3 of similar composition (aa 320-388) as in our own study , though others have failed
435 to detect direct binding (Pérez-rivas, Prieto, and Lozano 2010; Yin et al. 2009; Zhang et al.
436 1997). On the other hand, the structure of KSR1 has been resolved, with a shallow Cer binding
437 pocket identified based on similarity to other C1 domains to involve particularly residues L342,
438 V345, M353, I354 and F355 (M. Zhou et al. 2002). Thus, the KSR1 CA3 would not be expected
439 to, on its own, interact with the fatty acid chain or to be able to extract lipids from membranes,
440 but rather to interact with lipid head-groups. However, the same group challenged the Cer-
441 binding ability of the CA3 domain though it should be noted that, in this case, a truncated CA3
442 (aa 334 to 377) was employed.

443 In the characterization of our probes, a surprising observation was that the most salient
444 change in the behavior of the KSR probes in response to Cer-modifying drugs was a change
445 in total cellular fluorescence. This is in contrast to similar phospholipid probes, which change
446 locations rather than total fluorescence. The effect was consistently observed in both induction
447 and depletion directions, across several drug treatments, including Myr, FumB1, Palm,
448 SMase, C6 and Genz (Figs 2, 3, 5). For Myr treatment, we confirmed it was not simply due to
449 toxicity (which often accompanies changing levels of Cer (Hannun and Obeid 2008)) as
450 cytosolic RFP levels were unchanged. Moreover, we tested different concentrations in pilot
451 studies and chose concentrations and timepoints where visible signs of toxicity were low or
452 not yet apparent. With SMase treatment, neither the DAG probes nor the PRKCZ or SET
453 probes reacted in such a manner (Fig 3, S3). As mentioned briefly above, a potential
454 explanation is that the CA3 domain might itself be somewhat unstable or prone to misfolding
455 and subject to certain level of degradation, and that membrane binding thus stabilizes the
456 protein, leading to a decrease in degradation and concomitant increase in total probe
457 fluorescence. Indeed, full-length KSR1 binds cytosolic chaperones Hsp70, 90 and 68,
458 (Stewart et al. 1999), and ubiquitination of KSR1 has been reported, though the site identified
459 was outside the CA3 domain (Matheny et al. 2004; Rinaldi et al. 2016). Moreover,
460 phosphorylation at both T274 and S392 were required to increase the half-life of KSR1 from
461 1hr to 6hr (Rinaldi et al. 2016). Such a fast turnover time is consistent with our results which
462 were observed even with treatments as short as 30 min. The PM re-localization accompanying
463 SMase treatment observed for both C-KSR and C-KSR-GS, is consistent with such a
464 hypothesis, but for Palm treatment for C-KSR and Palm, C6 and Genz treatments for C-KSR-
465 GS, PM recruitment was less obvious and instead a truly global fluorescence increase was
466 observed. Whether this reflects the simultaneous binding of several types of organellar
467 membranes that were not resolved at the confocal level (for example ER, mitochondria, Golgi
468 and endo-lysosomal all at the same time), or whether post-translational modifications such as
469 phosphorylation or ubiquitination, or chaperone binding might also be modified, increasing
470 stability also of the cytosolic fraction of the probe, will be important to define in future studies.

471 In addition to its potential influence on cellular probe behavior, an intrinsic instability,
472 or requirement for post-translational modification of the CA3 domain to efficiently bind Cer
473 could well explain the difficulties we encountered in detecting *in vitro* binding. In these studies,
474 the only significant binding scores was the surprising interaction of the N-KSR probe to
475 GlcCer-containing liposomes. Though unexpected, as interaction of full-length KSR1 to
476 GlcCer has to our knowledge not been reported, such a modification to the lipid specificity
477 interaction is consistent with the difference between N- and C- constructs to Palm, Genz as
478 well as phagocytic stimuli. Future studies with drugs or genetic manipulation of enzymes such

479 as glucosyl and galactosyl ceramidases or transporters such as TMEM16F (Suzuki et al. 2013)
480 would be useful to corroborate these finding and determine more precisely the specificity of
481 this probe for glycosylated Cer, or potentially phosphorylated Cer in the cellular context.
482 Though we could not unambiguously verify specific direct binding of our probes to Cer *in vitro,*
483 which was in part due to liposome instability, an effect of instability of the purified or solubilized
484 probe itself, or of a disruptive interaction between probe and liposome membranes cannot be
485 discounted. Indeed, liposome morphology in arrays exposed to lysates bearing PKC-C1(2) or
486 EGFP was much more consistent and less spots were lost, even with sphingolipid containing
487 liposomes. Nevertheless, in the few zones that did show typical liposome morphology,
488 qualitative evidence of Cer binding could still be gleaned. However, for future biochemical
489 analyses it would be worth to explore whether, for example, the creation of S392A mutants of
490 the C-KSR-GS construct, which lacks MEK-interaction domains that leads to nuclear
491 localization (Brennan et al. 2002), may improve probe stability in solution, allowing *in vitro* Cer-
492 binding to be more precisely measured. Despite these drawbacks, the examination of our 3
493 KSR1-based constructs under different stimuli demonstrated that these probes may each
494 have their own utility as such or serve as a basis for future studies dissecting Cer, and
495 potentially GlcCer, dynamics in cells. The exacerbated instability of C-KSR, which prevented
496 constitutive PM localization, proved in fact to be advantageous in the way that it allowed for a
497 greater dynamic range in response to Cer changes by Palm and SMase, and more salient PM
498 recruitment with a phagocytic stimulus than C-KSR-GS. Thus, like conditional instability
499 employed in nanobody engineering (Tang et al. 2016), a future design could build upon these
500 observations to include proteasome targeting signals which maybe less disruptive than the
501 current design to membrane homeostasis (L. Zhao et al. 2022) to obtain a sensitive on-off
502 biosensor for PM Cer.

503 Finally, our intriguing observations of the differential behavior of N-KSR and C-KSR-
504 GS during phagocytosis suggests that the two probes are indeed responding to different lipid
505 changes in the cell, though verification using chemical or genetic manipulation of key enzymes
506 and transporters that modify Cer and GlcCer will be instrumental in more firmly establishing
507 this. One important notion to consider moving forward is that such cytosolic probes will only
508 detect lipids that are present on the cytosolic leaflet, or only when luminal leaflets are exposed
509 to the cytosol for example as may occur during PM or lysosomal disruption, where SM probe
510 lysenin has recently contributed greatly to our understanding of the role of SM (and indirectly
511 Cer) in membrane repair and antigen cytosol transfer in dendritic cells (Niekamp et al. 2022;
512 Canton et al. 2021). Though several studies indicate that Cer readily flip-flops across lipid
513 bilayers (Goñi et al. 2005), this is less likely for complex sphingolipids such as GlcCer, and
514 trans-bilayer transporters might maintain or establish gradients in response to cellular signals

515 as occurs for PS (Williamson 2015). As such, changes such as the loss of N-KSR PM signal
516 might equally represent a loss of total GlcCer as it might simply reflect its removal from the
517 cytosolic leaflet, which could explain why global changes in HexCer was not detected by
518 lipidomic analysis, though compensating changes in GalCer could also provide an
519 explanation. However, that the exciting ER localization of C-KSR-GS upon certain conditions
520 is simply a result of misfolding is unlikely, and investigation of whether this truly represents
521 Cer flux is ongoing in our laboratory. Although clearly more work will be required to define the
522 behavior and lipid specificity of these novel biosensors, we believe these constructs represent
523 useful new tools to explore sphingolipid regulation and function in living cells.

524

525 **Materials and Methods**

526 *Reagents*

527 The following antibodies (antibody Name/catalog #/dilution) were from: Abcam (USA) – anti-
528 Rab7/ ab137029/1:100; anti-Rab5/ab18211/1:100; Enzo Life Sciences (USA) – anti-LAMP1/
529 ADI-VAM-EN001/1:50, BD Biosciences (USA) – anti-TGN38/ 610898 /1:200; Thermo - AF555
530 Goat anti-mouse IgG/ A-21422/1:500, AF555-goat-anti-rabbit IgG/A-21428/1:250; Santa-Cruz
531 Biotechnology - Goat anti-rabbit IgG-HRP/1:5000, BioRad (USA) – Goat anti-mouse IgG-
532 HRP/170-6516/1:3000. The following lipids were purchased from: Avanti (USA, Sigma/Merck)
533 (Name/catalog #): DOPC/ 850375P, POPC/ 850457P, DOPS/ 840035P, POPE/850757P, PE-
534 PEG350/880430, C18 Ceramide/ 860518P, C18 Dihydroceramide/860627P,
535 Sphingosine/860490P, Diacylglycerol 18:1/800811O; Sphingomyelin from egg yolk/85615,
536 ceramide mix from bovine spinal cord/22244, Cholesterol/C8667. PE-Atto647/ AD 647N-161
537 was from Atto-Tec (Germany). All lipid standards were from Avanti (Sigma/Merck) amounts
538 given per 6-cm cell culture dish: DLPC (12:0-12:0 PC, 0.4 nmol/dish, cat. #850335), PE31:1
539 (17:0-14:1 PE, 1 nmol/dish, cat # LM-1104), PI31:1 (17:0-14:1 PI, 1 nmol/dish, cat # LM-1504),
540 PS31:1 (17:0-14:1 PS, 3.3 nmol/dish, cat# LM-1304), CL56:0 (14:0 Cardiolipin, 0.7 nmol/dish,
541 cat#710332), C12SM (C12 Sphingomyelin d18:1-12:0, 0.1 nmol/dish, cat#860583), C17Cer
542 (C17 Ceramide, d18:1-17:0, 2.5 nmol/dish, cat #860517), C8GC (C8 Glucosyl(B)Ceramide,
543 d18:1-8:0, 0.5 nmol/dish, cat#860540). Chemicals were purchased from Sigma/Merck unless
544 otherwise stated, (Name/catalog #): HPLC grade Methanol/4860-1L-R, HPLC grade
545 Chloroform/650471, tert-Butyl Methyl Ether (MTBE)/650560, Methylamine/534102; LC-MS
546 grade water/1153331000. Thermo: HPLC grade n-butanol/11378197. Plasmids used and
547 generated in this study are listed in Supplementary Table 1.

548 *DNA cloning*

549 All newly made constructs were verified by sequencing. Constructs expressing candidate
550 ceramide probes were constructed by subcloning fragments encoding human KSR1 (aa 317-
551 400, XM_047436985), N-terminal fragment of human PRKCZ(aa 123-193 , NM_002744.6),
552 20 kD C-terminal fragment human PRKCZ (aa 405-646), or human SET(aa 70-226,
553 NM_001122821.2) into pEGFP-N1 using restriction sites NheI and XhoI or into pEGFP-C1
554 using XhoI and KpnI sites to create C- or N-terminally tagged proteins, respectively. Tandem
555 2x-C-KSR probe was made by subcloning human KSR1(317-400) fragment encoding a
556 flexible linker sequence (GGSSGGGGA) into pKSR1-EGFP using XhoI and KpnI sites. The
557 sequence encoding Nuclear Export Signal (NES) from mammalian MAPKK kinase –
558 LQKKLEELEL was inserted by site directed mutagenesis (Q5 Site-Directed Mutagenesis Kit,
559 NEB, USA) after the start codons of human PRKCZ(405-646) or SET(70-226) to yield
560 plasmids pC-NES-C20-PRKCZ-EGFP and pC-NES-SET-EMD-EGFP, respectively. A point
561 mutation in the CA3 domain of KSR1 (C359S, C362S) with substitution of the two conserved
562 cysteines with serine residues was introduced using the Q5 Site-Directed Mutagenesis Kit.
563 For protein purification from *E.coli,* the human KSR1(aa 317-400) fragment was cloned into
564 SfiI restriction sites of the pETM11-SUMO3-sfGFP (Saliba et al. 2014) to make pETM11-
565 SUMO3-sfGFP-KSR1. The sequence encoding KSR1(317-400)-GFP was subcloned into
566 pETM11-SUMO3 via Gibson assembly using Gibson Assembly Cloning Kit (NEB, USA).
567 Sequences encoding N- or C-terminally tagged KSR1(317-400) were subcloned into SfiI sites
568 of pSBbi-pur-H-2Kb (# 111623, Addgene, USA) replacing H-2kb fragment. Primers used are
569 listed in Supplementary Table 2.

570 *Cell culture, transfection, and stable cell line establishment*

571 Wild-type mouse embryonic fibroblasts (MEF, ATCC CRL-2991), HeLa cells (ECACC,
572 93021013, a gift from N. Demaurex), and HEK 293T (HEK, ATCC-CRL-11268, a gift from N.
573 Demaurex) were cultured in DMEM (22320, Thermo), MEM (41090, Thermo) and DMEM
574 glutaMAX (31966, Thermo) respectively, containing 10% fetal bovine serum (FBS, Thermo),
575 1% pen/strep (10000 U/ml penicillin, 10 mg/ml streptomycin, PAN Biotech, Germany). JAWS
576 II (JAWS, ATCC CRL-11904) were grown in alpha minimum essential medium with
577 ribonucleosides,Deoxyribonucleosides (Gibco 22571), supplemented with 4 mM L-glutamine
578 (Gibco 25030), 1 mM sodium pyruvate (Gibco 58636), 5 ng/ml GM-CSF (Peprotech, 315-03)
579 20% FBS, 1% pen/strep. Delipidated FBS was prepared by incubating FBS with 0.5 g/ml lipid
580 removal beads (13358-U, Sigma/Merck) at 4°C overnight with rotation followed by
581 centrifugation (27000g, 20 min, 4°C) and supernatant filtration using 0.2 μm PES filters
582 (Nalgene). All cell lines were cultured at 37°C, 5% CO2, and passaged 1-2 times per week,
583 and used between passages 10 and 40. All cell lines were tested every 6-12 months either by
584 PCR (LookOut kit, Sigma/Merck) or Mycostrips (Invivogen, ep-mysnc-50) and were negative.

585 Cells were transfected upon reaching 60-70% confluency 2-3 days after seeding using
586 Lipofectamine 2000 (Thermo) in full culture medium without antibiotics for 4-6h. To prepare
587 DNA-lipofectamine complexes, equal volumes of serum- and antibiotic-free media containing
588 DNA or Lipofectamine were mixed and incubated at room temperature for 1h. To obtain stable
589 cell lines via transposition, MEF cells were first co-transfected with pSBbi-pur plasmids
590 encoding the protein of interest and pCMV-(CAT)T7-SB100 plasmid (#34879, Addgene, USA)
591 encoding Sleeping Beauty transposase SB100x. Puromycin (10 µg/mL) selection was
592 performed 2 days after co-transfection. Stable cell lines (N-KSR1 and C-KSR1) were
593 maintained in full culture medium containing puromycin (10 µg/ml). JAWS transfection was
594 achieved using 20 µg DNA and 20 x 10^6 million cells per 100 µl nucleofection solution from
595 the Amaxa Nucleofector Mouse Dendritic Cell kit (Lonza), and the Y-001 program. Cells were
596 diluted in 400 µl RPMI 1640 Glutamax medium, 25 mM HEPES medium (Thermo, 72400021)
597 immediately after electroporation, incubated for 10 min at RT, then centrifuged at 200 g, 5 min,
598 RT and resuspended in warm full medium and incubated overnight before imaging.

599 *Immunofluorescence*

600 MEF and HeLa cells seeded on 0.17 mm glass coverslips (Carl Roth) were fixed with 4%
601 paraformaldehyde (PFA, AlfaAesar) in PBS for 30 min at RT followed by 3X washes in PBS.
602 JAWS were fixed in 1%PFA for 10 min. For staining nuclei, fixed cells were incubated with 10
603 µg/ml Hoechst 33342 (Thermo) for 5 min at followed by three washes with PBS and mounting.
604 For immunostainings, cells were permeabilized with 0.1% Triton X-100 (in PBS) for 5 min at
605 RT, washed 3X by PBS, quenched with 25 mM Glycine/PBS for 10 min at RT, treated with
606 Image-IT-FX (Thermo) for 30 min followed by blocking with 2% bovine serum albumin
607 (BSA)/PBS for 30 min. After that the cells were incubated with primary antibodies at 4°C
608 overnight and with a secondary antibody for 1h in dark humid chambers, antibodies diluted in
609 blocking buffer. 3x washes in PBS were carried out between each step in the procedure.
610 Finally, the coverslips were mounted onto glass slides using 5 µl of ProLong Diamond
611 Mounting medium (Thermo) per coverslip. For labeling recycling endosomes, MEF cells were
612 incubated for 30 min at 37°C with 50 µg/ml Alexa555-conjugated human transferrin (Thermo)
613 in MEF full culture medium containing 0.2% (BSA). After 2x washed with PBS, cells were fixed
614 with 3% PFA for 20 min, quenched with 50 mM ammonium chloride for 15 min (RT), followed
615 by 3 washes in PBS and mounting. For staining the lysosomal lumen, MEF cells stably
616 expressing C-KSR were incubated overnight with 1 µg/ml Alexa Fluor 594 Hydrazide (Thermo)
617 in full culture medium with puromycin. The following day, medium was changed 5x to full
618 culture medium without Alexa 594 and the dye was chased for 2.5h before the start of
619 phagocytosis. Images were acquired either using Zeiss LSM700 or LSM800 confocal systems
620 /Plan apochromat 63x/1.4 objectives and Zeiss Zen 2010b version service pack1, or Nipkow

621 Okagawa Nikon spinning disk confocal imaging system Plan Apo 63x/1.4 DICIII objective and
622 Visiview 4.0 software (Visitron Systems).

623 *Drug treatments*

624 To induce sphingolipid depletion MEF cells were treated with: 0.5 μM myriocin (or methanol
625 vehicle) from *Mycelia sterilia* in full culture medium, with 2.5 μM fumonisin B1 (methanol
626 vehicle) from *Fusarium moniliforme* in culture medium containing 10% FBS delipidated as
627 above for 3 days, or with 10 μM fumonisin B1 in regular cell culture medium overnight. To
628 induce sphingolipid production MEF cells were treated with 0.5 mM BSA-conjugated palmitic
629 acid complex (Cayman Chemical, USA) for 4h at 37°C in delipidated-FBS medium, and in
630 regular medium with 100 μM Genz-123346 (DMSO vehicle) overnight, or 200 μM C6-ceramide
631 (d18:1/6:0) (Avanti/Merck) for 2h (ethanol vehicle). To induce DAG accumulation cells were
632 treated with 10 μM ionomycin in regular medium for 10 min. To release ceramides locally at
633 the plasma membrane cells were treated with 0.5 U/ml sphingomyelinase from
634 *Staphylococcus aureus* for 30 min in DMEM medium without FBS and antibiotics. After
635 treatment cells were either placed on ice, scraped and used for lipid extraction or fixed with
636 4% PFA and mounted for microscopy. Alternatively, after SMase treatment, cells were stained
637 with a sphingomyelin probe EGFP-Lysenin (Kiyokawa et al. 2005) (purified from *E.coli,* see
638 below) at 20 μg/ml in serum-free medium for 30 min at 37°C followed by 2 washed in PBS and
639 fixation as described above.

640 *Image analysis*

641 Image analysis was performed using ImageJ v1.52 (Schneider, Rasband, and Eliceiri 2012)
642 NIH. Colocalization analysis was conducted using the JACoP v2.0 plugin (Bolte and
643 Cordelières 2006) that returned Mander's coefficients for each region of interest (ROI). For
644 quantification of KSR probe fluorescence levels at the PM, ROIs for cells and background
645 were drawn manually or using Wand tool when possible on single confocal planes. The Make
646 Band... command, set to 2 μm width was used to transform the whole-cell ROIs into a PM
647 ROIs. Mean fluorescence intensities were measured from background-subtracted images.
648 Analyses determining the percentage of cells displaying plasma membrane localization were
649 conducted on images randomized by the Filename_Randomizer.txt macro
650 https://imagej.nih.gov/ij/macros/Filename_Randomizer.txt, by a blinded experimenter that
651 counted the number of PM-positive cells and total cells in each image using the Cell Counter
652 plugin. For whole-cell fluorescence intensity analyses, confocal z-stacks of 9 frames spaced
653 at 0.5 μm were acquired and sum projections of stacks were created using the Z-Projection
654 tool. Cell and background ROIs were drawn as above on the sum projections images to obtain
655 mean total cellular fluorescence intensities.

656 *Immunoblotting*

657 Cells grown to 80-90% confluency on 6-cm dishes were washed 3x with PBS, scraped off,
658 pelleted, and lysed in RIPA buffer (Thermo 89900) with protease inhibitors (Halt Protease
659 Inhibitor cocktail, 87785) for 30 min at 4°C. Cell debris was pelleted at max speed for 10 min
660 (4°C), and the supernatant was used for loading into the gel. Protein concentration was
661 quantitated using RotiQuant kit (Carl Roth). Lysates were diluted in the SDS Loading Buffer
662 (Roti-Load, Carl Roth) and heated at 95°C for 5 min. 15-30 µg protein were loaded and
663 separated by SDS-PAGE in 4–12% SurePAGE 12-well pre-cast gels (Genscript). Proteins
664 were transferred onto PVDF membranes using iBlot or iBlot2 system (Thermo). After transfer,
665 membranes were blocked in 5%milk/TBS-1%Tween-20 (TBST) for 1h (RT, agitation) followed
666 by incubation with primary antibodies diluted in 3%-milk/TBST overnight at 4°C and 1h
667 incubation at RT with HRP-conjugated secondary antibodies 3%-milk/TBST with multiple
668 washes in PBS between incubations with primary and secondary antibodies. Signals were
669 detected using Immobilon HRP substrate (Merck) on the ImageQuant LAS 4000 mini imaging
670 system (GE, USA).

671 *Lipid extraction and lipidomics*

672 For lipidomics experiments, lipids were extracted following a modified MTBE protocol (Guri et
673 al. 2017). MEF cells grown to confluency in lipid-free or full culture medium on 6-cm dishes
674 were washed in cold PBS and scraped off in 1 ml PBS. 900 µl and 100 µl cell suspension were
675 transferred to two separate tubes and the cells were pelleted at 400g for 5 min (4°C). The
676 pellets were kept at -80°C or used for protein quantitation (100 µl sample) by resuspension in
677 RIPA buffer, using RotiQuant as above, or for lipid extraction (900 µl sample) as follows. First,
678 pellets were resuspended in 100 µl LC-MS grade water, then 360 µl methanol and the lipid
679 standard mix (see Reagents section) were added, and the tubes vigorously vortexed. Next,
680 1.2 ml MTBE was added, and the samples were incubated for 1h at RT with shaking. 200 µl
681 of water was added to induce phase separation; samples were incubated at RT for 10 min
682 followed by centrifugation at 1000g, 10 min (RT). The upper organic phase was transferred to
683 13mm glass tube, 400 µl of the artificial upper phase (MTBE/methanol/water (10:3:1.5, v/v))
684 was added, the phase separation was repeated, and the collected second upper phase was
685 combined with the first one. The total lipid extract was divided into 2 equal parts: one for
686 sphingolipids (SL) and one for glycerophospholipids (TL). Extracts were dried in a speed
687 vacuum concentrator. After drying, the samples were flushed with nitrogen unless used for
688 further steps. The sphingolipid aliquot was treated with methylamine to remove phospholipids
689 by de-acylation (Clarke method (Clarke and Dawson 1981)). 0.5 mL monomethylamine
690 reagent (MeOH/H2O/n-butanol/Methylamine solution (4:3:1:5 v/v) was added to the dried

691 lipids, tubes sonicated for 6 min, vortexed, followed by the incubation for 1h at 53°C. Finally,
692 the methylamine-treated fraction was dried (as mentioned above). The monomethylamine-
693 treated lipids were subjected to desalting via extraction with *n*-butanol. In short, 300 µl water-
694 saturated *n*-butanol (*n*-butanol/water 2:1 v/v, mixed and prepared at least 1 day before use)
695 was added to the dried lipids. The samples were vortexed and sonicated for 6 min, and 150
696 µl LC-MS grade water was added. The mixture was vortexed thoroughly and centrifuged at
697 3200 x g for 10 min. The upper phase was transferred to a 2 mL amber vial. The lower phase
698 extraction was repeated as described above twice more, and the organic phases were
699 combined and dried.

700 Targeted lipidomic analysis by mass spectrometry was performed according to prior protocols
701 (Jiménez-Rojo et al. 2020) as follows: TL and SL aliquots were resuspended either in 250 µl
702 Chloroform: Methanol (LC-MS grade, 1:1 v/v) or directly in the sample solvent
703 ((Chloroform/Methanol/Water (2:7:1 v/v) + 5mM Ammonium Acetate). After sonication for 6
704 min (RT), lipid mixtures were transferred into wells of a 96-well Twin tech PCR plate
705 (Eppendorf) using Hamilton syringes. Sphingolipid aliquots were diluted 1:4, and total lipids
706 were diluted 1:10 in the sample solvent. PCR plate was sealed with EasyPierce foil (Thermo),
707 and the samples were injected into the TSQ Vantage Triple Stage Quadrupole mass
708 spectrometer (Thermo Fisher Scientific) equipped with a robotic sample handler and nanoflow
709 ion source Nanomate HD (Advion Biosciences, USA). The collision energy was optimized for
710 each lipid class. Lipid detection parameters are listed in Supplementary Table 3. Samples
711 were injected at a gas pressure of 30 psi with a spray voltage of 1.2 kV and run on the mass
712 spectrometer operated with a spray voltage of 3.5 kV for positive mode and 3.0 kV for negative
713 mode and a capillary temperature set at 190oC. Sphingolipid and glycerophospholipid species
714 were identified and quantified using multiple reaction monitoring (MRM). Cer species were
715 also quantified with a loss of water in the first quadrupole. Each biological replicate was
716 measured twice (2 technical replicates, TR). Each TR consisted of 3 measurements for each
717 transition. Each lipid species was quantified using standard curves created from internal
718 standards. Data analysis was performed using R version 3.6.2 (R Foundation for Statistical
719 Computing). The values where then normalized to the total lipid content of each corresponding
720 lipid extract (mol% of the sum of total PC, PE, PI, PS), except for samples of phagocytosing
721 cells, were lipid concentrations were normalized first to total protein of each corresponding
722 individual sample, then to the average of the sum of total PC, PE, PI, PS for the entire sample
723 group as explained in the results section.

724 *Protein purification from E.coli*

725 Rosetta 2(DE3) *E.coli* cells (Novagen) were transformed with the plasmids expressing His6-
726 SUMO3 tagged KSR probes or GFP alone (control): pETM11-His6-SUMO3- -sfGFP-N-KSR,
727 pETM11-His6-SUMO3-C-KSR-sfGFP, pETM11-His6-SUMO3-sfGFP. Transformed bacteria
728 were grown at 37°C in 1L LB medium containing 100 µg/ml kanamycin, 34 µg/ml
729 chloramphenicol until OD600 0.6-0.8. Protein expression was induced by the overnight
730 incubation with 0.4 mM Isopropyl β-D-thiogalactoside (IPTG) at 16°C. The next day cells
731 bacteria were lysed using the Microfluidizer LM20 high-pressure homogenizer (15000 psi
732 pressure, 2 cycles) in lysis buffer (50 mM Tris pH 7.5, 500 mM NaCl, 20 mM imidazole,
733 protease inhibitors (1 tablet/50 mL), 0.5 mM DTT) and the soluble fraction was obtained by
734 centrifugation at 16000g for 1h (4°C). Proteins harboring the His6 tag were captured by
735 incubation with Ni-NTA resin (Qiagen) (2ml resin per bacterial lysate from 1L culture) for 2h,
736 4°C, 30 rpm rotation. Agarose resin with bound proteins was centrifuged at 1200 rpm, 8 min
737 (4°C), and the slurry was transferred to a column with a cotton filter. The column was washed
738 with 20 ml Lysis buffer, His6-tagged proteins were eluted with 6 ml Elution Buffer (50 mM Tris
739 pH 7.5, 250 mM NaCl, 500 mM imidazole), DTT was added to 5 mM to prevent protein
740 aggregation. Eluted proteins were dialyzed against 50 mM Tris pH 7.5, 200 mM NaCl, 1 mM
741 DTT overnight at 4°C. The His6-SUMO3 tag was cleaved off the proteins by incubation with
742 His-tagged SenP2 protease (EMBL Protein Expression and Purification Core Facility
743 European, Germany) at a molar ratio of SenP2 to protein 40:1. The undigested proteins and
744 the protease were removed using Ni-NTA resin, purified proteins were eluted by applying
745 Elution Buffer 2 (50 mM Tris pH 7.5, 250 mM NaCl, 10 mM imidazole) to Ni-NTA-packed
746 column. The quality of purification was assessed by SDS-PAGE followed by Coomassie
747 staining (RotiBlue kit, CarlRoth). sfGFP-N-KSR was further purified by size exclusion
748 chromatography on the S75 column pre-equilibrated with 50 mM mM Tris, pH 7.4 and 250 mM
749 NaCl.

750 *Cell lysate preparation from HEK cells*

751 HEK cells grown on 10-cm dishes in HEK full culture medium to 70-80% confluency were
752 transfected as above with plasmids encoding EGFP (control), KSR lipid probes, or PKC-
753 C1(2)-GFP, where 20 µg plasmid DNA/50 µl lipofectamine 2000 was used per dish. After
754 overnight incubation, the cells were trypsinized for 1 min (RT) and resuspended in PBS
755 containing 0.5 mM EDTA. Cells suspension was centrifuged 200g, 5 min (4°C), followed by a
756 wash in PBS. After pelleting, cells were resuspended in 120 µl hypotonic lysis buffer (10 mM
757 Tris-HCl, pH=7.5, Halt protease and phosphatase inhibitors) and incubated on ice for 20 min.
758 Cells were lysed by passing the suspension 15 times through a 30G syringe needle. Protein
759 concentration was measured using a NanoDrop (Thermo). Finally, NaCl and DTT were added
760 to 150 mM and 5 mM, respectively.

761

762 *Liposome Microarray-based assay (LiMA)*

763 Liposome-based protein-lipid interaction assay was performed following the protocol
764 described in (Saliba et al. 2014). Lipid mixtures of different compositions were prepared in
765 chloroform: methanol: water (20:9:1 v/v). Lipid mixtures containing fluorescent lipid PE-
766 Atto647 (0.5 mol %) were spotted onto thin agarose layers covered by the protective
767 membrane on top of a glass slide using automated lipid spotting under an inert atmosphere
768 (Automatic TLC-spotter4, Camag, Switzerland). A microfluidic chamber with four channels
769 was manufactured from poly(dimethylsiloxane) PDMS, as described in (Saliba et al. 2014).
770 Then the agarose layers with spotted lipids were glued onto PDMS chambers using a 2:1
771 mixture of silicone elastomer: curing agent diluted 3× (v:v) in hexane as an adhesive, so the
772 resulting microfluidic chamber contained four channels of 30 spots, 120 lipid spots per
773 chamber. Liposomes were generated by manually injecting the liposome buffer (10 mM
774 HEPES, 150 mM NaCl) into each channel with a Hamilton syringe. Then, 40 µl of the solution
775 containing purified proteins at 5-10 µM (or HEK cell lysates) in liposome buffer with 5 mM DTT
776 were injected into channels using an automated injection system with a flow rate of 8 µl/min.
777 After incubation of freshly formed liposomes with the GFP-tagged proteins for 1h at RT, the
778 channels were manually washed with 80 µl of liposome buffer, and all spots in the chamber
779 were imaged with the Zeiss Axio Observer Z1 video time-lapse system. All images were taken
780 with the 20x objective; liposomes were imaged with the Cy5 filter set (5 and 10 ms exposure),
781 and GFP-tagged proteins were imaged at different exposure times (1, 5, 10, 25, 50, 75, 100,
782 150, 200, and 300 ms). Images were analyzed using a CellProfiler version 4.2.5 (Broad
783 Institute) custom pipeline described in detail in (Saliba et al. 2014). A Custom-made R script
784 was used to calculate the normalized binding intensity value (NBI) for each protein-lipid
785 interaction. NBI represents a mean of the ratio of GFP to Atto647 fluorescence divided by
786 exposure time at all exposure times for which spots were successfully segmented and is
787 proportional to the amount of GFP-tagged interaction protein recruited to the liposome surface.

788 *Preparation of phagocytic beads and phagocytosis*

789 3 µm carboxyl polystyrene beads (Spherotech, CP30-10) were covalently coupled with purified
790 human IgG (hIgG, Dunn Labortechnik, Germany) by washing 3 times in sterile PBS with
791 centrifugation at maximum speed (18,000 g) at 4°C, activating with 50 mM 1-Ethyl-3-(3-
792 dimethylaminopropyl) carbodiimide hydrochloride (EDC-HCl, Carl Roth/2156.1) for 15 min in
793 PBS at room temperature (RT) with rigorous shaking, followed by 3 washes at 4°C in 0.1 M
794 Na2B4O7 buffer (pH 8.0). Finally, 2 µg/µl of hIgG (and 15 ng/µl iFluor647-amine (AAT
795 Bioquest), for fluorescent beads) were added to the beads and incubated overnight at 4°C on

796 a shaker. Next day, the beads were washed 2x with 250 mM glycine/PBS followed by two
797 washes in PBS. To render MEF cells phagocytic MEF cells were transfected with 1 µg/2x10^5
798 cells pcDNA3-myc-FCGR2A (Fc receptor) plus KSR probes and where indicated TagRFP-
799 KDEL, mCherry-STIM1 or mCherry-Sec22b at 0.3 µg per 2x10^5 cells. Cells were washed in
800 full medium 4-6h after transfection. The following day beads were added to the cells at a bead-
801 to-cell ratio 10:1, cells were centrifuged at 200g, 2 min, RT, incubated with the beads for the
802 indicated times at 37°C, washed with PBS, fixed with 4% PFA/PBS for 30 min followed by 3x
803 washes with PBS and mounting as described above.

804

805 **Statistics and reproducibility**

806

807 All statistical analyses were done using Prism (GraphPad Software). P values that are
808 significant are shown above the bars. Two-tailed unpaired t-test were performed when
809 comparing two samples, Welch's correction was used if F test showed a significant difference
810 in variance. For three or more sample comparisons a one-way ANOVA was employed with in
811 case of negative F test, and Brown-Forsythe and Welch test in case F test showed significant
812 difference in variance, with Dunnett's post-hoc test. For lipidomic data multiple ratio paired t-
813 test was performed with a two-stage step-up method (Benjamini, Krieger, and Yekutieli), with
814 a false discovery rate set at 5%. Categorical quantification of plasma membrane recruitment
815 was performed by a blinded experimenter on randomized images. Contingency tables were
816 analysed using a Chi-squared test. Cells exhibiting abnormal morphology (multinucleated,
817 high vacuolation) or signs of death (blebbing) were excluded from analysis. A minimum of 5
818 replicate fields per coverslip are imaged for analysis of fixed cells. These may contain from 1
819 to tens of cells or 1 to tens of phagosomes which are considered as replicate values.

820

821 **Data availability**

822 Full datasets, including all microscopy and Western blot source images will be made available
823 on the University of Geneva's FAIR-compliant data repository Yareta under a CC BY 4.0
824 licence upon publication. Plasmids generated in this study will be deposited on Addgene upon
825 publication, to be distributed subject to a standard Material's Transfer Agreement.

826

827 **Acknowledgements**

828 We are grateful to the bioimaging and proteins and peptides core facilities at the University of
829 Geneva Medical Centre, Faculty of Medicine as well as the mass spectrometry core facility at

the Faculty of Science for their invaluable help. Thanks to Drs. Nicolas Demaurex, Maud Frieden, Brenda Kwak and Amado Carreras-Sureda for their valuable advice. This work was funded by a Professor Dr. Max Cloëtta Foundation Medical Researcher Grant (to PNH), a Swiss National Science Foundation grant (310030_189094, to PNH), a Schmidheiney Foundation subsidy (2022) to PNH. HR acknowledges the Swiss National Science Foundation (310030_184949), the NCCR Chemical Biology (51NF40-185898) and the Leducq Foundation. ACG. and LVE. acknowledge the financial support of the Louis-Jeantet Foundation, Switzerland.

Author Contributions

VG designed and performed experiments, analysed data and wrote the manuscript. LVE, IDQ, MA and MCC designed and performed experiments and analysed data. IR, and MM performed experiments and analysed data. HR and ACG designed experiments, provided guidance on analysis and interpretation of data as well as materials. PNH conceived the project, designed and performed experiments and wrote the manuscript.

Competing Interests

The authors declare no competing interests.

References

Abdel Shakor, Abo Bakr, Katarzyna Kwiatkowska, and Andrzej Sobota. 2004. "Cell Surface Ceramide Generation Precedes and Controls FcgammaRII Clustering and Phosphorylation in Rafts." *The Journal of Biological Chemistry* 279 (35): 36778–87. https://doi.org/10.1074/jbc.M402170200.

Abe, Mitsuhiro, and Toshihide Kobayashi. 2014. "Imaging Local Sphingomyelin-Rich Domains in the Plasma Membrane Using Specific Probes and Advanced Microscopy." *Biochimica et Biophysica Acta - Molecular and Cell Biology of Lipids* 1841 (5): 720–26. https://doi.org/10.1016/j.bbalip.2013.07.003.

Adachi, Yoshifumi, George N. Pavlakis, and Terry D. Copeland. 1994. "Identification and Characterization of SET, a Nuclear Phosphoprotein Encoded by the Translocation Break Point in Acute Undifferentiated Leukemia." *Journal of Biological Chemistry* 269 (3): 2258–62. https://doi.org/10.1016/s0021-9258(17)42162-4.

Albi, E., and M. P. Viola Magni. 1997. "Chromatin Neutral Sphingomyelinase and Its Role in Hepatic Regeneration." *Biochemical and Biophysical Research Communications* 236

(1): 29–33. https://doi.org/10.1006/BBRC.1997.6803.

Avota, Elita, Erich Gulbins, and Sibylle Schneider-Schaulies. 2011. "DC-SIGN Mediated Sphingomyelinase-Activation and Ceramide Generation Is Essential for Enhancement of Viral Uptake in Dendritic Cells." *PLoS Pathogens* 7 (2). https://doi.org/10.1371/journal.ppat.1001290.

Bakrač, Biserka, Aleš Kladnik, Peter Maček, Gavin McHaffie, Andreas Werner, Jeremy H. Lakey, and Gregor Anderluh. 2010. "A Toxin-Based Probe Reveals Cytoplasmic Exposure of Golgi Sphingomyelin." *Journal of Biological Chemistry* 285 (29): 22186–95. https://doi.org/10.1074/jbc.M110.105122.

Bidlingmaier, Scott, Kevin Ha, Nam Kyung Lee, Yang Su, and Bin Liu. 2016. "Proteome-Wide Identification of Novel Ceramide-Binding Proteins by Yeast Surface Cdna Display and Deep Sequencing." *Molecular and Cellular Proteomics* 15 (4): 1232–45. https://doi.org/10.1074/mcp.M115.055954.

Bjørnestad, Victoria Ariel, and Reidar Lund. 2023. "Pathways of Membrane Solubilization: A Structural Study of Model Lipid Vesicles Exposed to Classical Detergents." *Langmuir* 39 (11): 3914–33. https://doi.org/10.1021/acs.langmuir.2c03207.

Bockelmann, Svenja, John G.M. Mina, Sergei Korneev, Dina G. Hassan, Dagmar Müller, Angelika Hilderink, Hedwich C. Vlieg, et al. 2018. "A Search for Ceramide Binding Proteins Using Bifunctional Lipid Analogs Yields CERT-Related Protein StarD7." *Journal of Lipid Research* 59 (3): 515–30. https://doi.org/10.1194/jlr.M082354.

Bodman-Smith, Katherine B, Rachel E Gregory, Patrick T Harrison, and John G Raynes. 2004. "FcγRIIa Expression with FcγRI Results in C-Reactive Protein- and IgG-Mediated Phagocytosis." *Journal of Leukocyte Biology* 75 (6): 1029–35. https://doi.org/10.1189/jlb.0703306.

Bolte, S., and F. P. Cordelières. 2006. "A Guided Tour into Subcellular Colocalization Analysis in Light Microscopy." *Journal of Microscopy* 224 (3): 213–32. https://doi.org/10.1111/j.1365-2818.2006.01706.x.

Botelho, Roberto J., Mary Teruel, Renee Dierckman, Richard Anderson, Alan Wells, John D. York, Tobias Meyer, and Sergio Grinstein. 2000. "Localized Biphasic Changes in Phosphatidylinositol-4,5-Bisphosphate at Sites of Phagocytosis." *Journal of Cell Biology* 151 (7): 1353–67. https://doi.org/10.1083/jcb.151.7.1353.

Brennan, Jennifer A., Deanna J. Volle, Oleg V. Chaika, and Robert E. Lewis. 2002. "Phosphorylation Regulates the Nucleocytoplasmic Distribution of Kinase Suppressor of Ras." *Journal of Biological Chemistry* 277 (7): 5369–77. https://doi.org/10.1074/jbc.M109875200.

Buchberger, Amanda Rae, Kellen DeLaney, Jillian Johnson, and Lingjun Li. 2018. "Mass Spectrometry Imaging: A Review of Emerging Advancements and Future Insights." *Analytical Chemistry* 90 (1): 240–65. https://doi.org/10.1021/acs.analchem.7b04733.

902 Canals, Daniel, Silvia Salamone, and Yusuf A. Hannun. 2018. "Visualizing Bioactive
903 Ceramides." *Chemistry and Physics of Lipids* 216 (September): 142–51.
904 https://doi.org/10.1016/j.chemphyslip.2018.09.013.

905 Canton, Johnathan, Hanna Blees, Conor M Henry, Michael D Buck, Oliver Schulz, Neil C
906 Rogers, Eleanor Childs, et al. 2021. "The Receptor DNGR-1 Signals for Phagosomal
907 Rupture to Promote Cross-Presentation of Dead-Cell-Associated Antigens." *Nature*
908 *Immunology* 22 (2): 140–53. https://doi.org/10.1038/s41590-020-00824-x.

909 Chen, Xiaoying, Jennica L. Zaro, and Wei Chiang Shen. 2013. "Fusion Protein Linkers:
910 Property, Design and Functionality." *Advanced Drug Delivery Reviews* 65 (10): 1357.
911 https://doi.org/10.1016/J.ADDR.2012.09.039.

912 Clarke, N. G., and R. M. Dawson. 1981. "Alkaline O Leads to N-Transacylation. A New
913 Method for the Quantitative Deacylation of Phospholipids." *Biochemical Journal* 195
914 (1): 301. https://doi.org/10.1042/BJ1950301.

915 Codazzi, Franca, Mary N. Teruel, and Tobias Meyer. 2001. "Control of Astrocyte Ca2+
916 Oscillations and Waves by Oscillating Translocation and Activation of Protein Kinase
917 C." *Current Biology* 11 (14): 1089–97. https://doi.org/10.1016/S0960-9822(01)00326-8.

918 Contreras, F. Xabier, Jesús Sot, Alicia Alonso, and Félix M. Goñi. 2006. "Sphingosine
919 Increases the Permeability of Model and Cell Membranes." *Biophysical Journal* 90 (11):
920 4085–92. https://doi.org/10.1529/biophysj.105.076471.

921 Deng, Yaqin, Lin You, Yong Lu, Sungwon Han, Jingcheng Wang, Nikitha Vicas, Chuo
922 Chen, and Jin Ye. 2021. "Identification of TRAMs as Sphingolipid-Binding Proteins
923 Using a Photoactivatable and Clickable Short-Chain Ceramide Analog." *Journal of*
924 *Biological Chemistry* 297 (6): 101415. https://doi.org/10.1016/j.jbc.2021.101415.

925 Devaux, Philippe F. 1991. "Static and Dynamic Lipid Asymmetry in Cell Membranes."
926 *Biochemistry* 30 (5): 1163–73.
927 https://doi.org/10.1021/BI00219A001/ASSET/BI00219A001.FP.PNG_V03.

928 Ekman, Peik, Terhi Maula, Shou Yamaguchi, Tetsuya Yamamoto, Thomas K.M. Nyholm,
929 Shigeo Katsumura, and J. Peter Slotte. 2015. "Formation of an Ordered Phase by
930 Ceramides and Diacylglycerols in a Fluid Phosphatidylcholine Bilayer - Correlation
931 with Structure and Hydrogen Bonding Capacity." *Biochimica et Biophysica Acta -*
932 *Biomembranes* 1848 (10): 2111–17. https://doi.org/10.1016/j.bbamem.2015.06.019.

933 Eva Fuglsang, Louise Boye, and Hanne Frokiaer. 2017. "Enhancement of Ceramide
934 Formation Increases Endocytosis of Lactobacillus Acidophilus and Leads to Increased
935 IFN-Beta and IL-12 Production in Dendritic Cells. ." *Journal of Clinical Immunology*
936 *Research* 1 (1): 1–9.

937 Gallegos, Lisa L, Maya T Kunkel, and Alexandra C Newton. 2006. "Targeting Protein
938 Kinase C Activity Reporter to Discrete Intracellular Regions Reveals Spatiotemporal
939 Differences in Agonist-Dependent Signaling." *The Journal of Biological Chemistry* 281

(41): 30947–56. https://doi.org/10.1074/jbc.M603741200.

Giodini, Alessandra, Christoph Rahner, and Peter Cresswell. 2009. "Receptor-Mediated Phagocytosis Elicits Cross-Presentation in Nonprofessional Antigen-Presenting Cells." *Proceedings of the National Academy of Sciences of the United States of America* 106 (9): 3324–29. https://doi.org/10.1073/pnas.0813305106.

Goñi, Félix M., and Alicia Alonso. 1999. "Structure and Functional Properties of Diacylglycerols in Membranes." *Progress in Lipid Research* 38 (1): 1–48. https://doi.org/10.1016/S0163-7827(98)00021-6.

Goñi, Félix M, F-Xabier Contreras, L-Ruth Montes, Jesús Sot, and Alicia Alonso. 2005. "Biophysics (and Sociology) of Ceramides." *Biochemical Society Symposium*, no. 72: 177–88. https://doi.org/10.1042/bss0720177.

Götz, Ralph, Tobias C. Kunz, Julian Fink, Franziska Solger, Jan Schlegel, Jürgen Seibel, Vera Kozjak-Pavlovic, Thomas Rudel, and Markus Sauer. 2020. "Nanoscale Imaging of Bacterial Infections by Sphingolipid Expansion Microscopy." *Nature Communications 2020 11:1* 11 (1): 1–9. https://doi.org/10.1038/s41467-020-19897-1.

Goulden, Brady D., Jonathan Pacheco, Allyson Dull, James P. Zewe, Alexander Deiters, and Gerald R.V. Hammond. 2019. "A High-Avidity Biosensor Reveals Plasma Membrane PI(3,4)P2 Is Predominantly a Class I PI3K Signaling Product." *Journal of Cell Biology* 218 (3): 1066–79. https://doi.org/10.1083/jcb.201809026.

Guido, Daniele, Nicolas Demaurex, and Paula Nunes. 2015. "Junctate Boosts Phagocytosis by Recruiting Endoplasmic Reticulum Ca 2 + Stores near Phagosomes," no. October: 4074–82. https://doi.org/10.1242/jcs.172510.

Guri, Yakir, Marco Colombi, Eva Dazert, Sravanth K. Hindupur, Jason Roszik, Suzette Moes, Paul Jenoe, et al. 2017. "MTORC2 Promotes Tumorigenesis via Lipid Synthesis." *Cancer Cell* 32 (6): 807-823.e12. https://doi.org/10.1016/J.CCELL.2017.11.011.

Hammond, Gerald R.V., Morgan M.C. Ricci, Claire C. Weckerly, and Rachel C. Wills. 2022. "An Update on Genetically Encoded Lipid Biosensors." *Molecular Biology of the Cell* 33 (5): 1–7. https://doi.org/10.1091/mbc.E21-07-0363.

Hannun, Yusuf A., and Lina M. Obeid. 2008. "Principles of Bioactive Lipid Signalling: Lessons from Sphingolipids." *Nature Reviews Molecular Cell Biology*. https://doi.org/10.1038/nrm2329.

———. 2018. "Sphingolipids and Their Metabolism in Physiology and Disease." *Nature Reviews Molecular Cell Biology*. Nature Publishing Group. https://doi.org/10.1038/nrm.2017.107.

Hinkovska-Galcheva, Vania, Laurence A Boxer, Andrei Kindzelskii, Miki Hiraoka, Akira Abe, Sravan Goparju, Sarah Spiegel, Howard R Petty, and James A Shayman. 2005. "Ceramide 1-Phosphate, a Mediator of Phagocytosis." *Journal of Biological Chemistry*

977 280 (28): 26612–21. https://doi.org/10.1074/jbc.M501359200.

978 Ivics, Zoltán, Meng Amy Li, Lajos Mátés, Jef D Boeke, Andras Nagy, Allan Bradley, and
979 Zsuzsanna Izsvák. 2009. "Transposon-Mediated Genome Manipulation in Vertebrates."
980 *Nature Methods* 6 (6): 415–22. https://doi.org/10.1038/nmeth.1332.

981 Jiménez-Rojo, Noemi, Manuel D. Leonetti, Valeria Zoni, Adai Colom, Suihan Feng, Namrata
982 R. Iyengar, Stefan Matile, et al. 2020. "Conserved Functions of Ether Lipids and
983 Sphingolipids in the Early Secretory Pathway." *Current Biology : CB* 30 (19): 3775-
984 3787.e7. https://doi.org/10.1016/J.CUB.2020.07.059.

985 Kiefer, Kerstin, Amado Carreras-Sureda, Roberto García-López, Fanny Rubio-Moscardó,
986 Josefina Casas, Gemma Fabriàs, and Rubén Vicente. 2015. "Coordinated Regulation of
987 the Orosomucoid-like Gene Family Expression Controls de Novo Ceramide Synthesis in
988 Mammalian Cells." *Journal of Biological Chemistry* 290 (5): 2822–30.
989 https://doi.org/10.1074/jbc.M114.595116.

990 Kiyokawa, Etsuko, Takeshi Baba, Naomi Otsuka, Asami Makino, Shinichi Ohno, and
991 Toshihide Kobayashi. 2005. "Spatial and Functional Heterogeneity of Sphingolipid-Rich
992 Membrane Domains." *Journal of Biological Chemistry* 280 (25): 24072–84.
993 https://doi.org/10.1074/JBC.M502244200.

994 Kjellberg, Matti A., Max Lönnfors, J. Peter Slotte, and Peter Mattjus. 2015. "Metabolic
995 Conversion of Ceramides in HeLa Cells - A Cholesteryl Phosphocholine Delivery
996 Approach." *PLoS ONE* 10 (11): 1–19. https://doi.org/10.1371/journal.pone.0143385.

997 Krishnamurthy, Kannan, Somsankar Dasgupta, and Erhard Bieberich. 2007. "Development
998 and Characterization of a Novel Anti-Ceramide Antibody." *Journal of Lipid Research*
999 48 (4): 968–75. https://doi.org/10.1194/jlr.D600043-JLR200.

1000 Kwiatkowska, Katarzyna, Renata Hordejuk, Piotr Szymczyk, Magdalena Kulma, Abo-Bakr
1001 Abdel-Shakor, Andrzej Płucienniczak, Krzysztof Dołowy, Adam Szewczyk, and
1002 Andrzej Sobota. 2007. "Lysenin-His, a Sphingomyelin-Recognizing Toxin, Requires
1003 Tryptophan 20 for Cation-Selective Channel Assembly but Not for Membrane Binding."
1004 *Molecular Membrane Biology* 24 (2): 121–34.
1005 https://doi.org/10.1080/09687860600995540.

1006 Levin, Roni, Sergio Grinstein, and Johnathan Canton. 2016. "The Life Cycle of Phagosomes:
1007 Formation, Maturation, and Resolution." *Immunological Reviews* 273 (1): 156–79.
1008 https://doi.org/10.1111/imr.12439.

1009 Levin, Roni, Sergio Grinstein, and Daniel Schlam. 2015. "Phosphoinositides in Phagocytosis
1010 and Macropinocytosis." *Biochimica et Biophysica Acta - Molecular and Cell Biology of*
1011 *Lipids* 1851 (6): 805–23. https://doi.org/10.1016/j.bbalip.2014.09.005.

1012 Lorent, J. H., K. R. Levental, L. Ganesan, G. Rivera-Longsworth, E. Sezgin, M. Doktorova,
1013 E. Lyman, and I. Levental. 2020. "Plasma Membranes Are Asymmetric in Lipid
1014 Unsaturation, Packing and Protein Shape." *Nature Chemical Biology* 16 (6): 644–52.

1015 https://doi.org/10.1038/s41589-020-0529-6.

1016 Magenau, Astrid, Carola Benzing, Nicholas Proschogo, Anthony S. Don, Leila Hejazi,
1017 Denuja Karunakaran, Wendy Jessup, and Katharina Gaus. 2011. "Phagocytosis of IgG-
1018 Coated Polystyrene Beads by Macrophages Induces and Requires High Membrane
1019 Order." *Traffic* 12 (12): 1730–43. https://doi.org/10.1111/j.1600-0854.2011.01272.x.

1020 Majeski, Amy E., and J. Fred Dice. 2004. "Mechanisms of Chaperone-Mediated Autophagy."
1021 *The International Journal of Biochemistry & Cell Biology* 36 (12): 2435–44.
1022 https://doi.org/10.1016/J.BIOCEL.2004.02.013.

1023 Mátés, Lajos, Marinee K L Chuah, Eyayu Belay, Boris Jerchow, Namitha Manoj, Abel
1024 Acosta-Sanchez, Dawid P Grzela, et al. 2009. "Molecular Evolution of a Novel
1025 Hyperactive Sleeping Beauty Transposase Enables Robust Stable Gene Transfer in
1026 Vertebrates." *Nature Genetics* 41 (6): 753–61. https://doi.org/10.1038/ng.343.

1027 Matheny, Sharon A, Chiyuan Chen, Robert L Kortum, Gina L Razidlo, Robert E Lewis, and
1028 Michael A White. 2004. "Ras Regulates Assembly of Mitogenic Signalling Complexes
1029 through the Effector Protein IMP." *Nature* 427 (6971): 256–60.
1030 https://doi.org/10.1038/nature02237.

1031 Mathias, Shalini, Louis A. Peña, and Richard N. Kolesnick. 1998. "Signal Transduction of
1032 Stress via Ceramide." *Biochemical Journal* 335 (3): 465–80.
1033 https://doi.org/10.1042/bj3350465.

1034 Merrill, Alfred H., M. Cameron Sullards, Elaine Wang, Kenneth A. Voss, and Ronald T.
1035 Riley. 2001. "Sphingolipid Metabolism: Roles in Signal Transduction and Disruption by
1036 Fumonisins." *Environmental Health Perspectives* 109 (SUPPL. 2): 283–89.
1037 https://doi.org/10.1289/ehp.01109s2283.

1038 Miyake, Y., Y. Kozutsumi, S. Nakamura, T. Fujita, and T. Kawasaki. 1995. "Serine
1039 Palmitoyltransferase Is the Primary Target of a Sphingosine-like Immunosuppressant,
1040 ISP-1/Myriocin." *Biochemical and Biophysical Research Communications* 211 (2):
1041 396–403. https://doi.org/10.1006/bbrc.1995.1827.

1042 Montes, L Ruth, M Begoña Ruiz-Argüello, Félix M Goñi, and Alicia Alonso. 2002.
1043 "Membrane Restructuring via Ceramide Results in Enhanced Solute Efflux." *The*
1044 *Journal of Biological Chemistry* 277 (14): 11788–94.
1045 https://doi.org/10.1074/jbc.M111568200.

1046 Mukhopadhyay, Archana, Sahar A. Saddoughi, Pengfei Song, Iyad Sultan, Suriyan
1047 Ponnusamy, Can E. Senkal, Christopher F. Snook, et al. 2009. "Direct Interaction
1048 between the Inhibitor 2 and Ceramide via Sphingolipid-Protein Binding Is Involved in
1049 the Regulation of Protein Phosphatase 2A Activity and Signaling." *FASEB Journal* 23
1050 (3): 751–63. https://doi.org/10.1096/fj.08-120550.

1051 Niekamp, Patrick, Gaelen Guzman, Hans C. Leier, Ali Rashidfarrokhi, Veronica Richina,
1052 Fabian Pott, Caroline Barisch, Joost C. M. Holthuis, and Fikadu G. Tafesse. 2021.

1053 "Sphingomyelin Biosynthesis Is Essential for Phagocytic Signaling during
1054 *Mycobacterium Tuberculosis* Host Cell Entry." Edited by Christina L. Stallings. *MBio*
1055 12 (1). https://doi.org/10.1128/mBio.03141-20.

1056 Niekamp, Patrick, Felix Scharte, Tolulope Sokoya, Laura Vittadello, Yeongho Kim,
1057 Yongqiang Deng, Elisabeth Südhoff, et al. 2022. "Ca2+-Activated Sphingomyelin
1058 Scrambling and Turnover Mediate ESCRT-Independent Lysosomal Repair." *Nature*
1059 *Communications* 13 (1). https://doi.org/10.1038/s41467-022-29481-4.

1060 Nunes-Hasler, Paula, Sophia Maschalidi, Carla Lippens, Cyril Castelbou, Samuel Bouvet,
1061 Daniele Guido, Flavien Bermont, et al. 2017. "STIM1 Promotes Migration, Phagosomal
1062 Maturation and Antigen Cross-Presentation in Dendritic Cells." *Nature Communications*
1063 8 (1): 1852. https://doi.org/10.1038/s41467-017-01600-6.

1064 Nunes, Paula, Daniela Cornut, Vanessa Bochet, Udo Hasler, Masatsugu Oh-Hora, Jean Marc
1065 Waldburger, and Nicolas Demaurex. 2012. "STIM1 Juxtaposes ER to Phagosomes,
1066 Generating Ca2+ Hotspots That Boost Phagocytosis." *Current Biology* 22 (21): 1990–
1067 97. https://doi.org/10.1016/j.cub.2012.08.049.

1068 Pathak, Divya, Neelay Mehendale, Shubham Singh, Roop Mallik, and Siddhesh S. Kamat.
1069 2018. "Lipidomics Suggests a New Role for Ceramide Synthase in Phagocytosis." *ACS*
1070 *Chemical Biology* 13 (8): 2280–87. https://doi.org/10.1021/acschembio.8b00438.

1071 Pédelacq, Jean Denis, Stéphanie Cabantous, Timothy Tran, Thomas C. Terwilliger, and
1072 Geoffrey S. Waldo. 2006. "Engineering and Characterization of a Superfolder Green
1073 Fluorescent Protein." *Nature Biotechnology* 24 (1): 79–88.
1074 https://doi.org/10.1038/nbt1172.

1075 Pérez-rivas, Luís G, Stephanie Prieto, and José Lozano. 2010. "1 . Modulation of Ras
1076 Signaling by the KSR Family of Molecular Scaffolds." *Emerging Signaling Pathways in*
1077 *Tumor Biology* 661 (2): 1–23. http://www.trnres.com/ebook/uploads//T_12700118641
1078 Lazo corrected.pdf.

1079 Pohl, Antje, Iván López-Montero, Florent Rouvière, Fabrice Giusti, and Philippe F. Devaux.
1080 2009. "Rapid Transmembrane Diffusion of Ceramide and Dihydroceramide Spin-
1081 Labelled Analogues in the Liquid Ordered Phase."
1082 *Http://Dx.Doi.Org/10.1080/09687680902733815* 26 (3): 194–204.
1083 https://doi.org/10.1080/09687680902733815.

1084 Quinville, Brianna M, Natalie M Deschenes, Alex E Ryckman, Jagdeep S Walia, N M ;
1085 Ryckman, and A E ; Walia. 2021. "Molecular Sciences A Comprehensive Review:
1086 Sphingolipid Metabolism and Implications of Disruption in Sphingolipid Homeostasis."
1087 https://doi.org/10.3390/ijms22115793.

1088 Razidlo, Gina L., Robert L. Kortum, Jamie L. Haferbier, and Robert E. Lewis. 2004.
1089 "Phosphorylation Regulates KSR1 Stability, ERK Activation, and Cell Proliferation."
1090 *Journal of Biological Chemistry* 279 (46): 47808–14.

1091 https://doi.org/10.1074/jbc.M406395200.

1092 Rinaldi, L, R Delle Donne, M Sepe, M Porpora, C Garbi, F Chiuso, A Gallo, et al. 2016.
1093 "Praja2 Regulates KSR1 Stability and Mitogenic Signaling." *Cell Death & Disease* 7
1094 (5): e2230. https://doi.org/10.1038/cddis.2016.109.

1095 Saharan, Ojal, Neelay Mehendale, and Siddhesh S. Kamat. 2022. "Phagocytosis: A
1096 (Sphingo)Lipid Story." *Current Research in Chemical Biology* 2 (March): 100030.
1097 https://doi.org/10.1016/j.crchbi.2022.100030.

1098 Saliba, Antoine Emmanuel, Ivana Vonkova, Stefano Ceschia, Greg M. Findlay, Kenji Maeda,
1099 Christian Tischer, Samy Deghou, et al. 2014. "A Quantitative Liposome Microarray to
1100 Systematically Characterize Protein-Lipid Interactions." *Nature Methods* 11 (1): 47–50.
1101 https://doi.org/10.1038/nmeth.2734.

1102 Sallusto, Federica, Chiara Nicolò, Ruggero De Maria, Silvia Corinti, and Roberto Testi.
1103 1996. "Ceramide Inhibits Antigen Uptake and Presentation by Dendritic Cells." *Journal*
1104 *of Experimental Medicine* 184 (6): 2411–16. https://doi.org/10.1084/jem.184.6.2411.

1105 Santos, Nina Criado, Samuel Bouvet, Flavien Bermont, Cyril Castelbou, Farah Mansour,
1106 Maral Azam, Francesca Giordano, and Paula Nunes-Hasler. 2022. "The SNARE Sec22b
1107 Regulates Phagosome Maturation by Promoting ORP8-Mediated PI(4)P Exchange at
1108 ER-Phagosome Contact Sites." *BioRxiv*, January, 2022.04.12.487993.
1109 https://doi.org/10.1101/2022.04.12.487993.

1110 Schneider, Caroline A., Wayne S. Rasband, and Kevin W. Eliceiri. 2012. "NIH Image to
1111 ImageJ: 25 Years of Image Analysis." *Nature Methods* 9 (7): 671–75.
1112 https://doi.org/10.1038/NMETH.2089.

1113 Schramm, Michael, Jasmin Herz, Albert Haas, Martin Krönke, and Olaf Utermöhlen. 2008.
1114 "Acid Sphingomyelinase Is Required for Efficient Phago-Lysosomal Fusion." *Cellular*
1115 *Microbiology* 10 (9): 1839–53. https://doi.org/10.1111/j.1462-5822.2008.01169.x.

1116 Scorrano, Luca, Maria Antonietta De Matteis, Scott Emr, Francesca Giordano, György
1117 Hajnóczky, Benoît Kornmann, Laura L. Lackner, et al. 2019. "Coming Together to
1118 Define Membrane Contact Sites." *Nature Communications* 10 (1): 1–11.
1119 https://doi.org/10.1038/s41467-019-09253-3.

1120 Shiraishi, Takayuki, Shinichiro Imai, and Yutaka Uda. 2003. "The Presence of Ceramidase
1121 Activity in Liver Nuclear Membrane." *Biological & Pharmaceutical Bulletin* 26 (6):
1122 775–79. https://doi.org/10.1248/BPB.26.775.

1123 Stewart, Scott, Meera Sundaram, Yanping Zhang, Jeeyong Lee, Min Han, and Kun-Liang
1124 Guan. 1999. "Kinase Suppressor of Ras Forms a Multiprotein Signaling Complex and
1125 Modulates MEK Localization." *Molecular and Cellular Biology* 19 (8): 5523–34.
1126 https://doi.org/10.1128/mcb.19.8.5523.

1127 Suzuki, Jun, Toshihiro Fujii, Takeshi Imao, Kenji Ishihara, Hiroshi Kuba, and Shigekazu

1128 Nagata. 2013. "Calcium-Dependent Phospholipid Scramblase Activity of TMEM16
1129 Protein Family Members." *The Journal of Biological Chemistry* 288 (19): 13305–16.
1130 https://doi.org/10.1074/jbc.M113.457937.

1131 Tafesse, Fikadu G., Ali Rashidfarrokhi, Florian I. Schmidt, Elizaveta Freinkman, Stephanie
1132 Dougan, Michael Dougan, Alexandre Esteban, Takeshi Maruyama, Karin Strijbis, and
1133 Hidde L. Ploegh. 2015. "Disruption of Sphingolipid Biosynthesis Blocks Phagocytosis
1134 of Candida Albicans." Edited by Alex Andrianopoulos. *PLoS Pathogens* 11 (10):
1135 e1005188. https://doi.org/10.1371/journal.ppat.1005188.

1136 Tang, Jonathan C Y, Eugene Drokhlyansky, Behzad Etemad, Stephanie Rudolph, Binggege
1137 Guo, Sui Wang, Emily G Ellis, Jonathan Z Li, and Constance L Cepko. 2016.
1138 "Detection and Manipulation of Live Antigen-Expressing Cells Using Conditionally
1139 Stable Nanobodies." Edited by Liqun Luo. *ELife* 5: e15312.
1140 https://doi.org/10.7554/eLife.15312.

1141 Tran, Thi Thu Trang, Bárbara Graziela Postal, Sylvie Demignot, Agnès Ribeiro, Céline
1142 Osinski, Jean Paul Pais De Barros, Agnieszka Blachnio-Zabielska, et al. 2016. "Short
1143 Term Palmitate Supply Impairs Intestinal Insulin Signaling via Ceramide Production."
1144 *The Journal of Biological Chemistry* 291 (31): 16328.
1145 https://doi.org/10.1074/JBC.M115.709626.

1146 Veiga, M. Pilar, José Luis R. Arrondo, Félix M. Goñi, and Alicia Alonso. 1999. "Ceramides
1147 in Phospholipid Membranes: Effects on Bilayer Stability and Transition to Nonlamellar
1148 Phases." *Biophysical Journal* 76 (1 I): 342–50. https://doi.org/10.1016/S0006-
1149 3495(99)77201-2.

1150 Vieira, O V, R J Botelho, L Rameh, S M Brachmann, T Matsuo, H W Davidson, A Schreiber,
1151 J M Backer, L C Cantley, and S Grinstein. 2001. "Distinct Roles of Class I and Class III
1152 Phosphatidylinositol 3-Kinases in Phagosome Formation and Maturation." *The Journal*
1153 *of Cell Biology* 155 (1): 19–25. https://doi.org/10.1083/jcb.200107069.

1154 Walter, T., J. Schlegel, A. Burgert, A. Kurz, J. Seibel, and M. Sauer. 2017. "Incorporation
1155 Studies of Clickable Ceramides in Jurkat Cell Plasma Membranes." *Chemical*
1156 *Communications* 53 (51): 6836–39. https://doi.org/10.1039/C7CC01220A.

1157 Wang, Guanghu, Kannan Krishnamurthy, Nagavedi S. Umapathy, Alexander D. Verin, and
1158 Erhard Bieberich. 2009. "The Carboxyl-Terminal Domain of Atypical Protein Kinase Cζ
1159 Binds to Ceramide and Regulates Junction Formation in Epithelial Cells." *Journal of*
1160 *Biological Chemistry* 284 (21): 14469–75. https://doi.org/10.1074/jbc.M808909200.

1161 Wang, Guanghu, Jeane Silva, Kannan Krishnamurthy, Eric Tran, Brian G Condie, and Erhard
1162 Bieberich. 2005. "Direct Binding to Ceramide Activates Protein Kinase Czeta before the
1163 Formation of a Pro-Apoptotic Complex with PAR-4 in Differentiating Stem Cells." *The*
1164 *Journal of Biological Chemistry* 280 (28): 26415–24.
1165 https://doi.org/10.1074/jbc.M501492200.

1166 Williamson, Patrick. 2015. "Phospholipid Scramblases." *Lipid Insights* 8 (Suppl 1): 41–44.
1167 https://doi.org/10.4137/LPI.S31785.

1168 Wu, Yuqing, Cao Li, Andrea Riehle, Barbara Pollmeier, Erich Gulbins, and Heike Grassmé.
1169 2018. "Mycobacterial Infection Is Promoted by Neutral Sphingomyelinase 2 Regulating
1170 a Signaling Cascade Leading to Activation of B1-Integrin." *Cellular Physiology and*
1171 *Biochemistry* 51 (4): 1815–29. https://doi.org/10.1159/000495683.

1172 Yamaji, A, Y Sekizawa, K Emoto, H Sakuraba, K Inoue, H Kobayashi, and M Umeda. 1998.
1173 "Lysenin, a Novel Sphingomyelin-Specific Binding Protein." *The Journal of Biological*
1174 *Chemistry* 273 (9): 5300–5306. https://doi.org/10.1074/jbc.273.9.5300.

1175 Yeung, Tony, and Sergio Grinstein. 2007. "Lipid Signaling and the Modulation of Surface
1176 Charge during Phagocytosis." *Immunological Reviews* 219 (1): 17–36.
1177 https://doi.org/10.1111/j.1600-065X.2007.00546.x.

1178 Yin, Xianglei, Mohammad Zafrullah, Hyunmi Lee, Adriana Haimovitz-Friedman, Zvi Fuks,
1179 and Richard Kolesnick. 2009. "A Ceramide-Binding C1 Domain Mediates Kinase
1180 Suppressor of Ras Membrane Translocation." *Cellular Physiology and Biochemistry* 24
1181 (3–4): 219–30. https://doi.org/10.1159/000233248.

1182 Zhang, Yuhua, Yao Bei, Sylvie Delikat, Shariff Bayoumy, Lin Xin-Hua, Subham Basu,
1183 Michael McGinley, Po Ying Chan-Hui, Henri Lichenstein, and Richard Kolesnick.
1184 1997. "Kinase Suppressor of Ras Is Ceramide-Activated Protein Kinase." *Cell* 89 (1):
1185 63–72. https://doi.org/10.1016/S0092-8674(00)80183-X.

1186 Zhao, Hongmei, Malgorzata Przybylska, I. Huan Wu, Jinhua Zhang, Craig Siegel, Svetlana
1187 Komarnitsky, Nelson S. Yew, and Seng H. Cheng. 2007. "Inhibiting Glycosphingolipid
1188 Synthesis Improves Glycemic Control and Insulin Sensitivity in Animal Models of Type
1189 2 Diabetes." *Diabetes* 56 (5): 1210–18. https://doi.org/10.2337/db06-0719.

1190 Zhao, Lin, Jia Zhao, Kunhong Zhong, Aiping Tong, and Da Jia. 2022. "Targeted Protein
1191 Degradation: Mechanisms, Strategies and Application." *Signal Transduction and*
1192 *Targeted Therapy* 7 (1): 113. https://doi.org/10.1038/s41392-022-00966-4.

1193 Zhou, Kecheng, Andrea Dichlberger, Hector Martinez-Seara, Thomas K.M. Nyholm, Shiqian
1194 Li, Young Ah Kim, Ilpo Vattulainen, Elina Ikonen, and Tomas Blom. 2018. "A
1195 Ceramide-Regulated Element in the Late Endosomal Protein LAPTM4B Controls
1196 Amino Acid Transporter Interaction." *ACS Central Science* 4 (5): 548–58.
1197 https://doi.org/10.1021/acscentsci.7b00582.

1198 Zhou, Ming, David A. Horita, David S. Waugh, R. Andrew Byrd, and Deborah K. Morrison.
1199 2002. "Solution Structure and Functional Analysis of the Cysteine-Rich C1 Domain of
1200 Kinase Suppressor of Ras (KSR)." *Journal of Molecular Biology* 315 (3): 435–46.
1201 https://doi.org/10.1006/jmbi.2001.5263.

1202

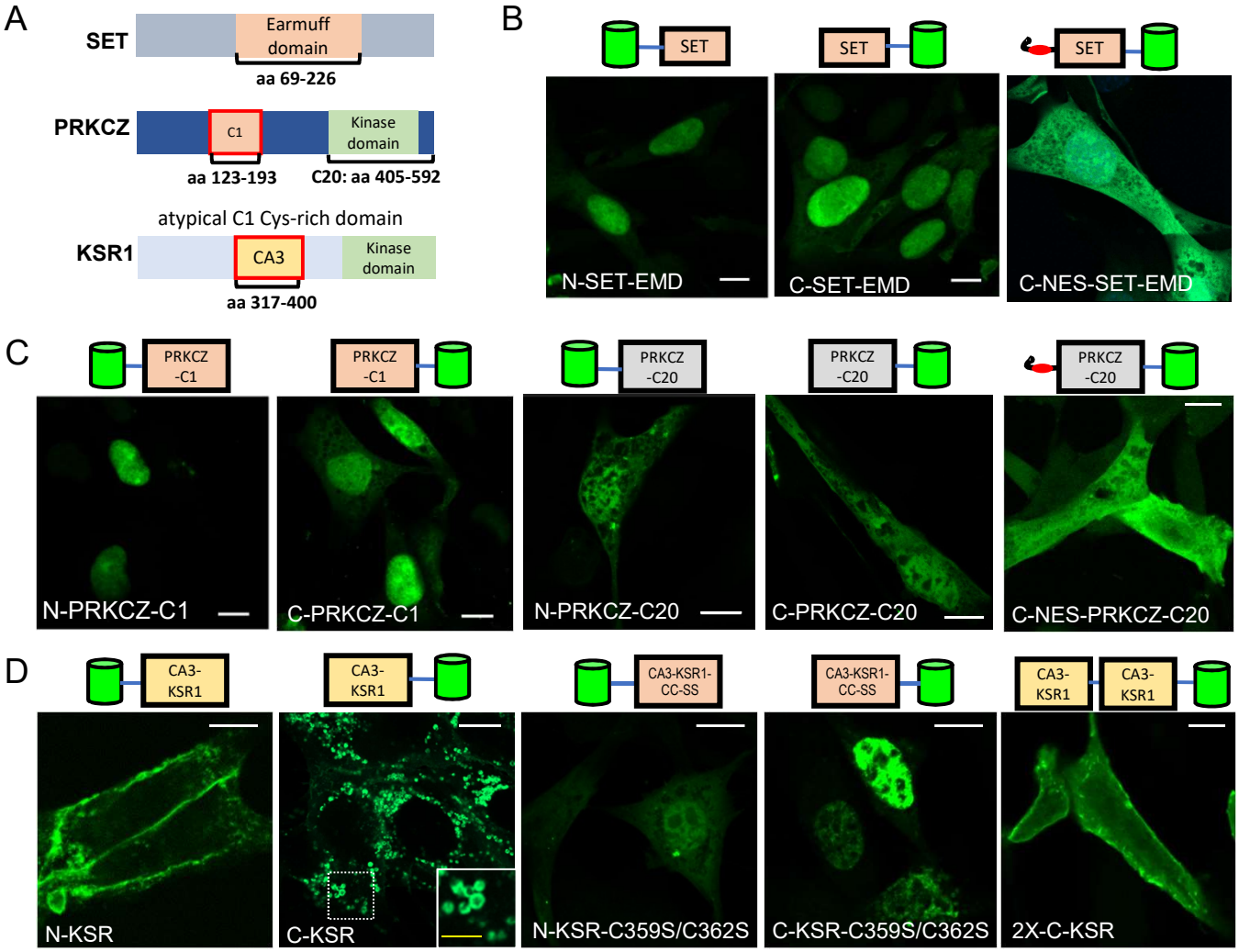

Figure 1. *Localization of candidate ceramide (Cer) probes in mouse embryonic fibroblasts (MEFs).* **A)** Schematic representation of Cer-binding domains used for probe construction from the following source proteins: Human SET earmuff domain (EMD), amino acids (as) 69-226; atypical PKC type zeta C1 domain (PRKCZ-C1, aa 123-193) and C20 domain (encompassing also the kinase domain, PRKCZ-C20 aa 405-592); and KSR1 CA3 domain (containing an atypical C1 domain, KSR, aa 317-400). **B-D)** Confocal images of MEF cells transfected with N-terminally (N-) or C-terminally (C-) EGFP-tagged Cer-binding domains of SET (B), PRKCZ (C) and KSR1 (D). Constructs preceded by a nuclear export signal are labelled NES, the tandem construct is labelled 2X and the cysteine mutants C359S/C362S. The inset in C-KSR highlights enlarged vesicular structures. White bars = 10 µm, yellow bar = 3 µm.

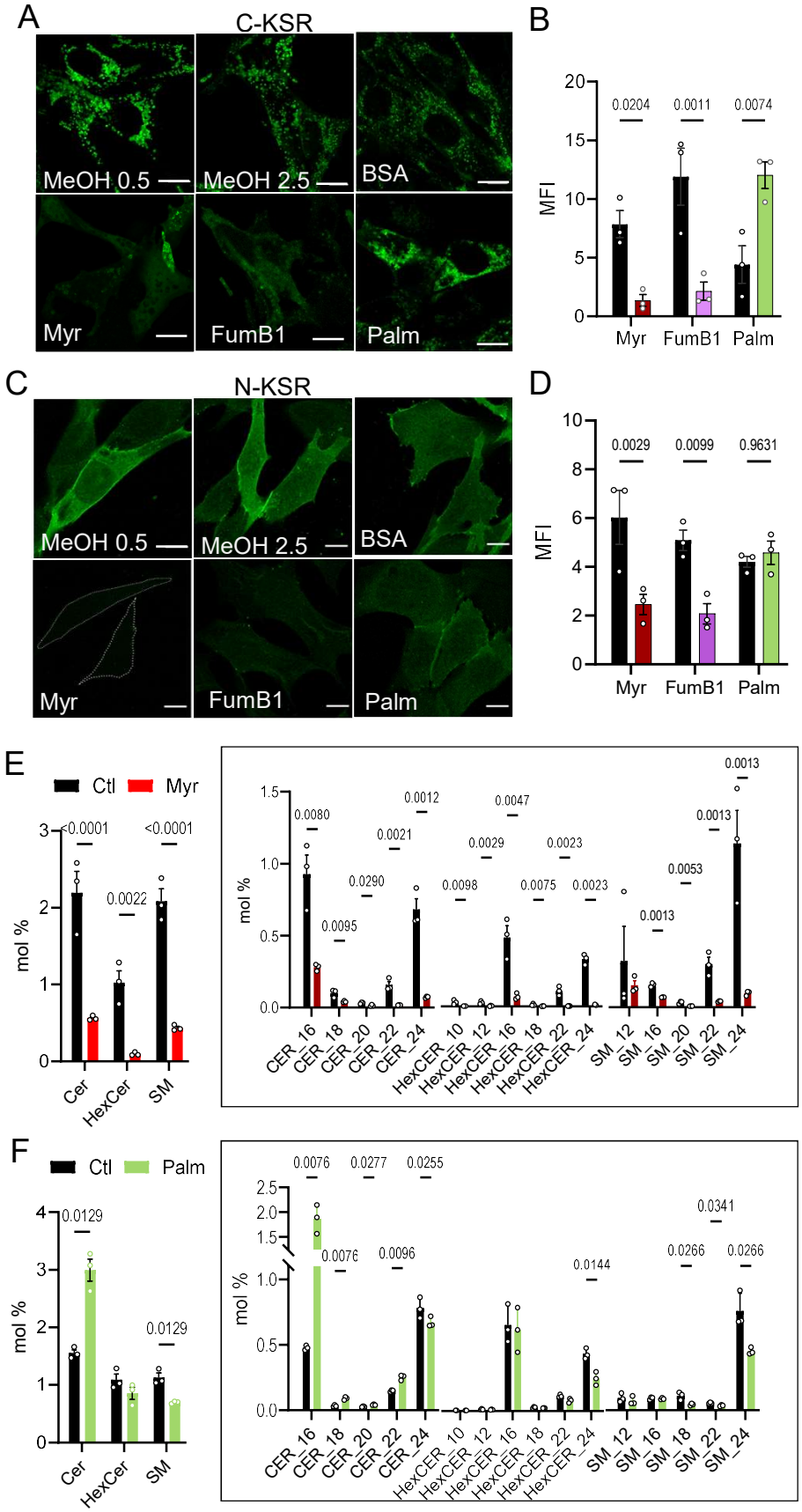

Figure 2. *Response of C- and N-KSR to Cer-modifying drugs.* **A, C)** Confocal images of MEF cells stably expressing C-KSR (A) or N-KSR (B) (in green) treated with; 0.5 μM myriocin (Myr) or 2.5 μM fumonisin B1 (FumB1) FumB1 for 3d; or 0.5 mM BSA-complexed palmitate (Palm) for 4h (bottom panels), and respective vehicle controls (top panels). **B-D)** Quantification of total cellular mean fluorescence intensity (MFI) of cells in A and C respectively. Bars are means +/- SEM, (n= 3 coverslips for each condition). White bars = 10 μm. **E)** Targeted lipidomic analysis of MEF cells stably expressing C-KSR, treated with Myr as above. Left panel shows the quantification of the sum total mass of lipids classified as ceramides (Cer), hexosyl-ceramides (HexCer), and sphingomyelins (SM), normalized to the total mass glycerophospholipids in the same sample (expressed as percent mole, %mol). Inset shows the quantification of the 5 most abundant Cer (left) HexCer (middle) and SM (right) species grouped by fatty acid chain length. **F)** Similar analysis as in **E)** of cells treated for 4h with Palm. Bars are means + SEM. (n=3, see also Table S1).

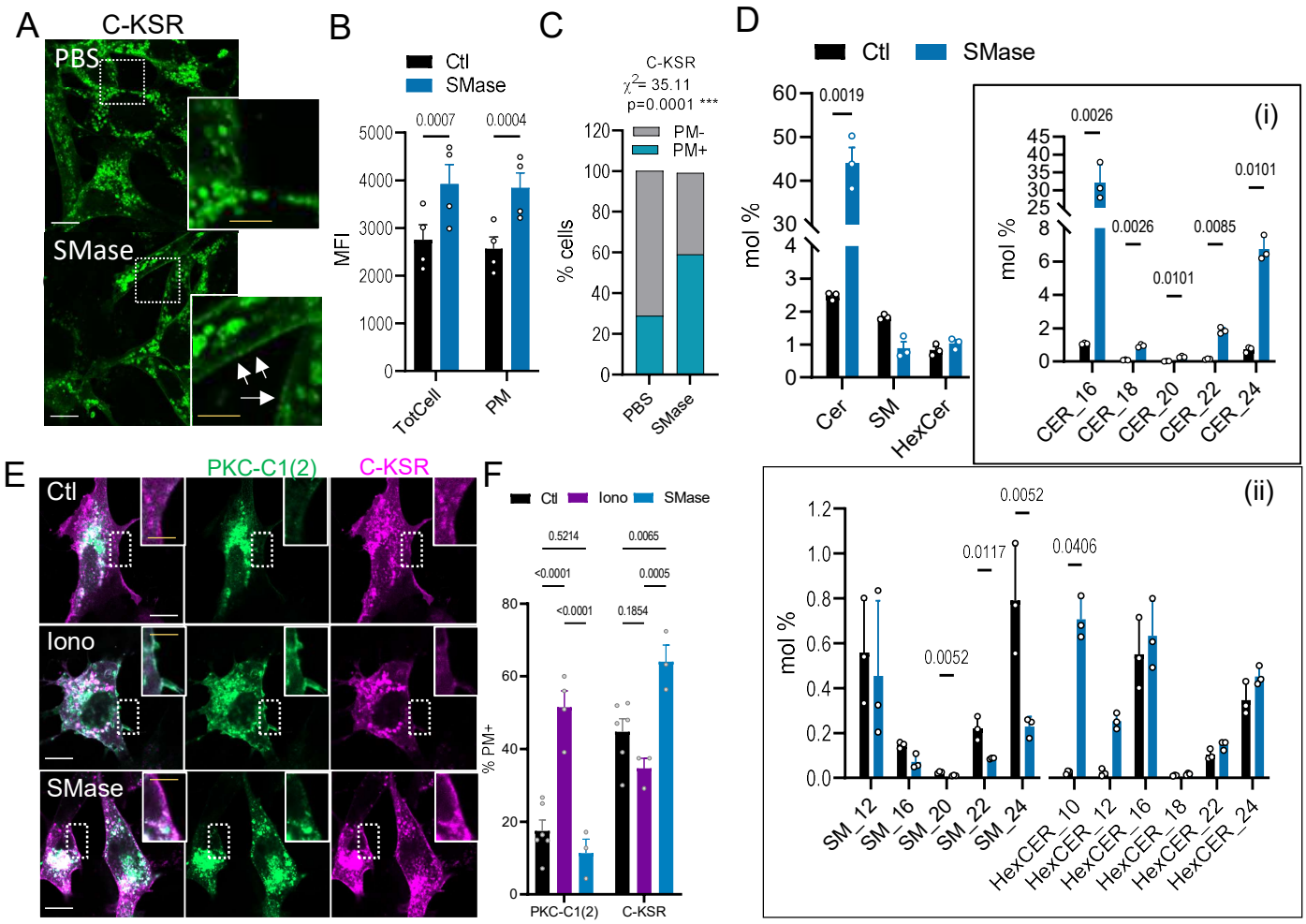

Figure 3. *C-KSR responds to Sphingomyelinase-induced Cer.* **A)** Confocal images of MEF cells stably expressing C-KSR (green) treated with 0.5 U/ml bacterial sphingomyelinase (SMase) or PBS control for 30 min. **B)** Quantification of total cellular MFI of cells in A), as well as fluorescence of the plasma membrane (PM) only of cells in A). (n=4 coverslips) **C)** Blinded quantification of the fraction of cells displaying PM localization in PBS or SMase-treated condition in A). (Pooled cells from n=4 coverslips is 170 PBS/202 SMase-treated) A-B). **D)** Targeted lipidomic analysis of MEF cells stably expressing C-KSR, treated with SMase as above. Left upper panel shows the quantification of the sum total Cer, HexCer, SM. Insets show the quantification of the 5 most abundant Cer (i) HexCer (ii, right) and SM (ii, left) species grouped by fatty acid chain length. (n=3, see also Table S1) **E)** Confocal images of MEF cells co-transfected with C-KSR-mRFP (magenta) and diacylglycerol (DAG) probe PCK-C1(2)-EGFP (green), control (Ctl, top) or treated with 10 μM ionomycin (Iono) for 10 min (middle), or with SMase as above (bottom). **F)** Blinded quantification of cells in E displaying PM localization of either C-KSR or PKC-C1(2) probe. (n= 6/3/3 for Ctl/Iono/SMase). Bars are means + SEM. White bars = 10 μm, yellow bar = 3 μm.

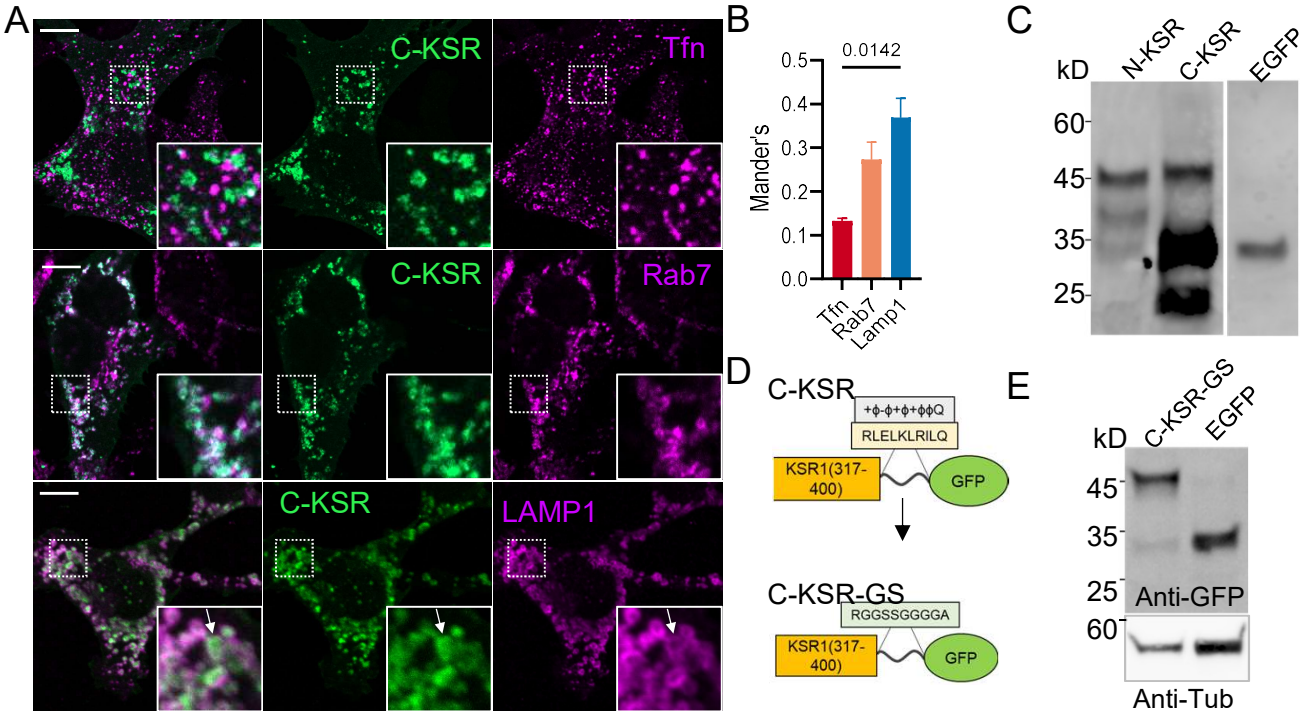

Figure 4. *Generation of a more stable C-KSR probe, C-KSR-GS.* **A)** Confocal images of MEF cells transfected with C-KSR (green) and loaded for 30 min with recycling endosome marker Alexa555-conjugated human transferrin (Tfn, 50 µg/ml, magenta top); or immunostained with late endosome marker anti-Rab7 (magenta middle) or lysosomal marker anti-LAMP1 (magenta bottom). The arrow points to an enlarged vesicular structure showing peripheral C-KSR localization with a hollow lumen, that is surrounded yet by LAMP1 staining. **B)** Quantification of co-localization between C-KSR and organelle marker, expressed as Mander's coefficient (n=4/4/14 coverslips for Tfn/Rab7/LAMP1). **C)** Western blot of lysates of MEF cells stably expressing C-KSR or N-KSR or transfected with cytosolic EGFP and probed with anti-GFP antibody. **D)** Schematic representation of the linker mutagenesis employed to create the new probe C-KSR-GS. **E)** Western blot of MEF cells transfected with either C-KSR-GS or EGFP, and stained first with anti-GFP, then re-probed with anti-tubulin (Tub). Bars are means + SEM. White bars = 10 µm, yellow bars = 3 µm.

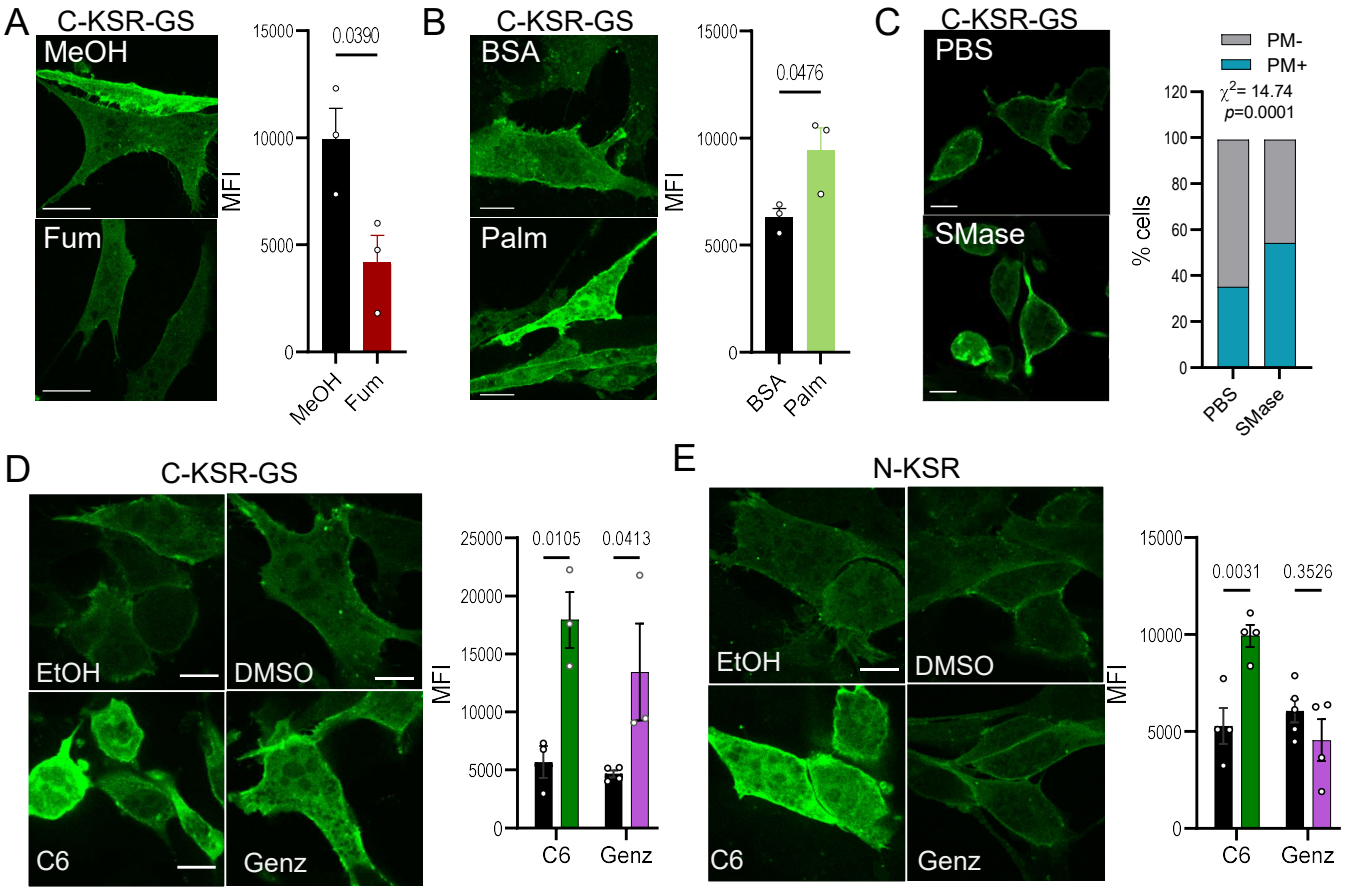

Figure 5. *C-KSR-GS responds to Cer modulation similarly to C-KSR.* **A-C)** Confocal images of MEFs transfected with C-KSR-GS and treated with 10 μM FumB1 (bottom) for 1d or methanol (MeOH) vehicle control (top) (A); 0.5 mM Palm for 4 h (bottom) or BSA control (top) (B); or 0.5 U/ml SMase for 30 min (bottom) or PBS control (top) (C). Right panels shows the quantification of total cellular fluorescence (MFI) (n=3 coverslips, for A-B) or blinded quantification of the fraction of cells displaying prominent PM localization (C, n=4 coverslips pooled, 168/237 cells PBS/SMase). **D-E)** Confocal images of MEFs expressing C-KSR-GS (D) or N-KSR (E) and treated (bottom) with either Cer analog C6 (200 μM, 2h, left) or 100 μM of the GlcCer synthase inhibitor Genz-123346 (Genz, 1d, right), or their respective ethanol (EtOH) or dimethylsulfoxide (DMSO) vehicle controls (top). Right panels show the quantification of total cellular fluorescence (MFI) (in D: n=3/3/4/3 coverslips for EtOH/C6/DMSO/Genz; in E: n = 4 coverslips for all conditions). Bars are means +(or +/-) SEM. White bars = 10 μm.

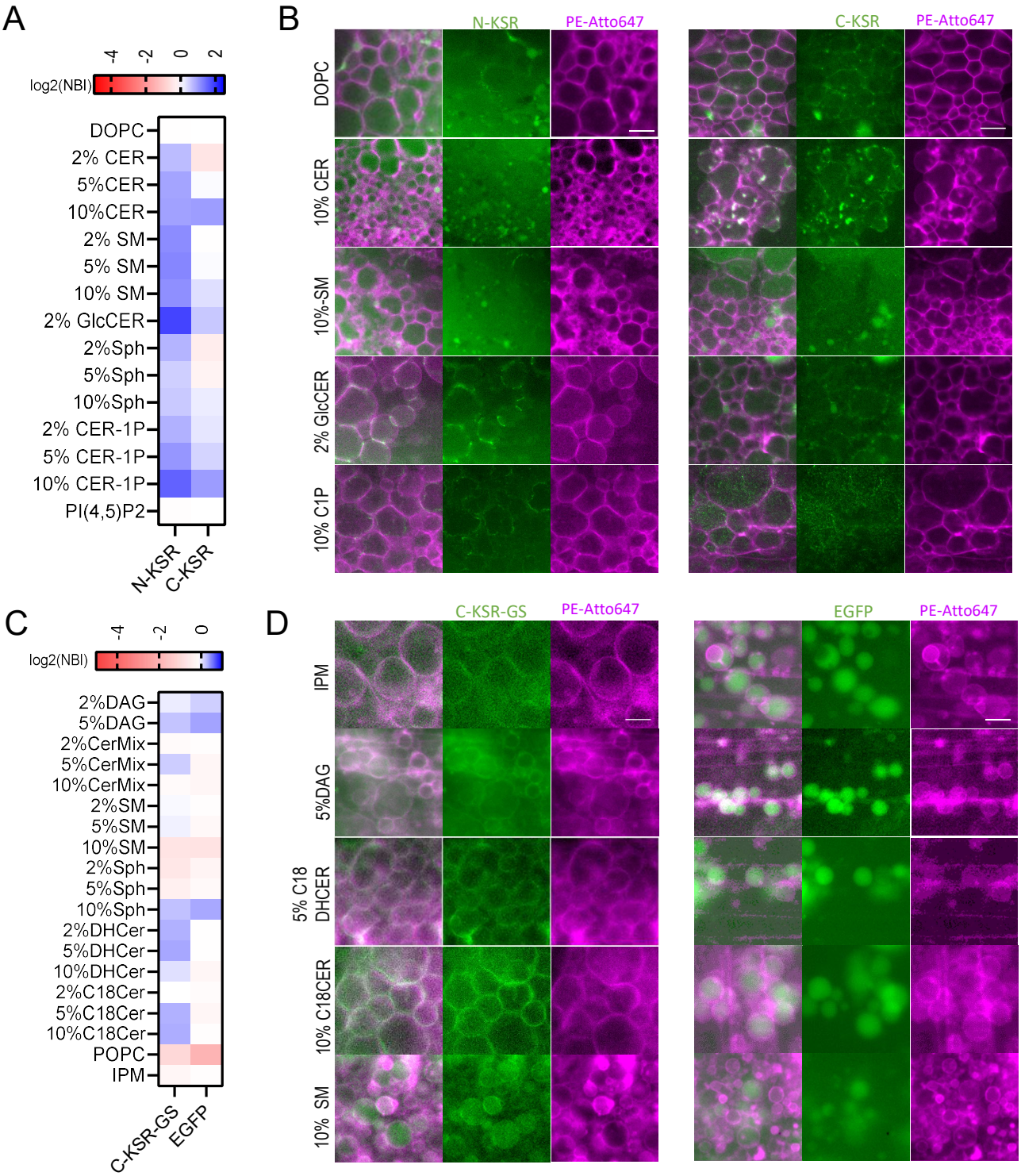

Figure 6. *Liposome microarray (LiMa) analysis of KSR probes.* **A)** Heatmap summarizing the automated quantification of liposome binding in LiMa analysis using purified N-KSR and C-KSR and DOPC-based liposomes. Values are expressed as Log(2) transformed ratios of the mean normalized binding indices (NBI) for each liposome compostion tested as compared to the corresponding score for DOPC liposomes alone (n=3/1-2 for N-KSR/C-KSR, see also Table S2) **B)** Representative epifluorescence images of liposome array spots showing liposome membranes labelled in PE-Atto647 (magenta) or probe fluorescence (green, N-KSR left, C-KSR right) **C)** Heatmap of LiMa analysis as in A) of C-KSR-GS or cytosolic EGFP obtained from HEK293 lysates and inner plasma membrane (IPM)-mimicking liposomes (n=2-6, see also Table S2). **D)** Representative epifluorescence images as in B) for C-KSR-GS (left) and EGFP (right), in the context of IPM liposomes (see also Fig S5) . White bars = 10 µm.

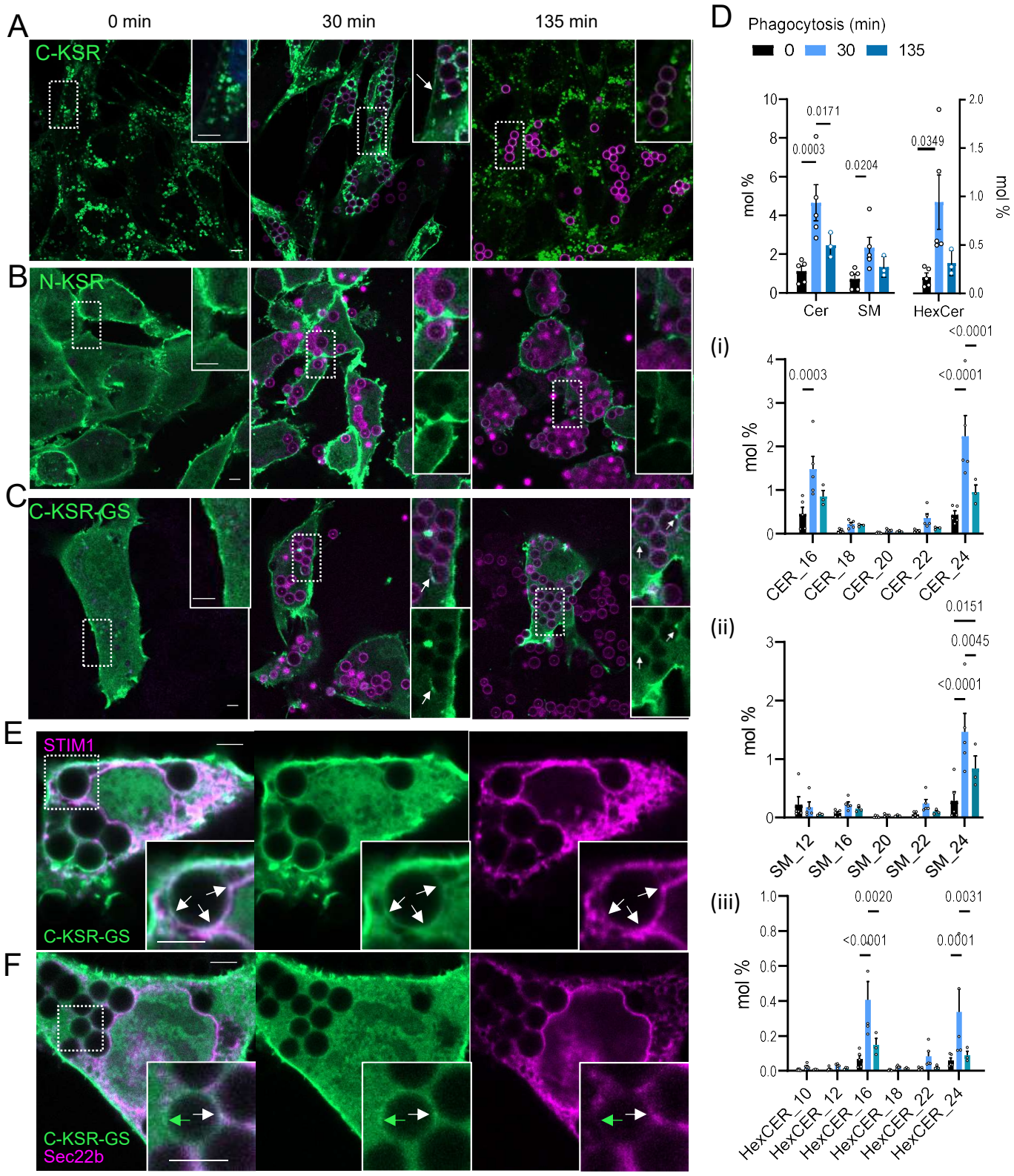

Figure 7. *Behavior of KSR probes during phagocytosis in MEFs.* **A-C)** Confocal images of phagocytic MEFs expressing (in green) C-KSR (A), N-KSR (B) and C-KSR-GS (C), exposed to IgG-Alexa647-coupled beads at 1:10 cell:bead ratio for 0 (left), 30 (middle) and 135 (right) min. **D)** Targeted lipidomic analysis of MEF cells stably expressing C-KSR, treated exposed to IgG-beads as above. Top panel shows the quantification of the sum total Cer, HexCer, SM. Quantification of the 5 most abundant species grouped by fatty acid chain length is shown for Cer (i) SM (ii) and HexCer (iii) species. (n=3, see also Table S3). **E-F)** Confocal images of phagocytic MEFs co-transfected with C-KSR-GS (green) and proteins known to localize to membrane contact sites between ER and phagosomes mCh-STIM1 (E, magenta) and mCh-Sec22b (F, magenta), and exposed to IgG-beads as above. White arrows show periphagosomal regions where overlap of fluorescent protein signal is discerned, green arrow shows regions with green fluorescence only. Bars are means +SEM. White bars = 3 µm.

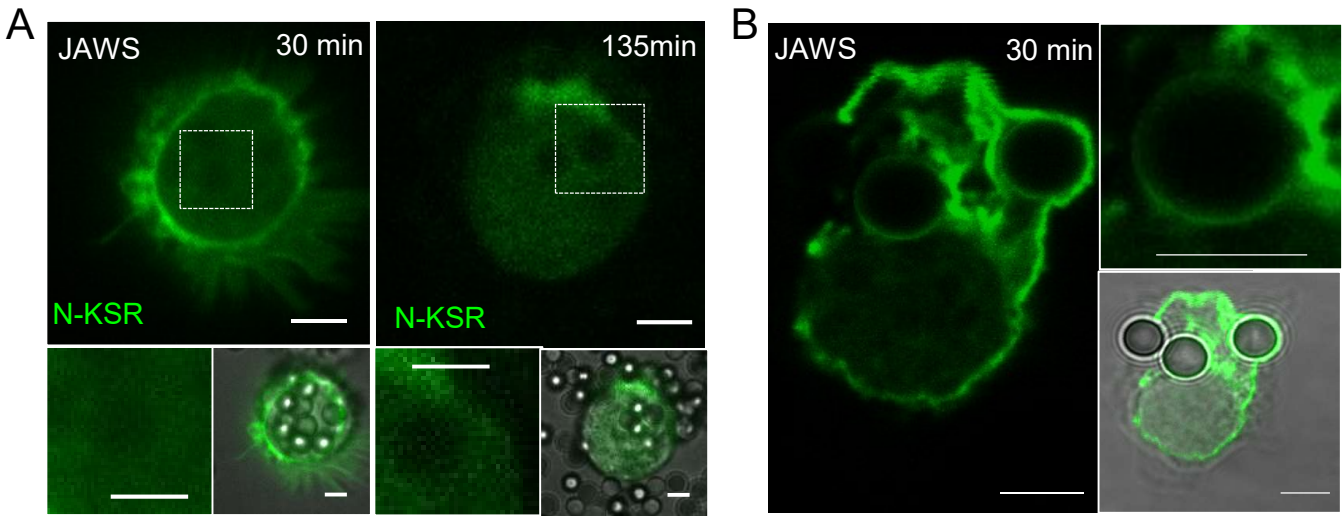

Figure 8. *Behavior of KSR probes during phagocytosis in dendritic cells.* **A-B)** Confocal images of dendritic cell line JAWS transfected with (in green) N-KSR (A) exposed to IgG-coupled beads at 1:10 cell:bead ratio for 30 (left) and 135 (right) min, and C-KSR-GS (B) exposed to beads for 30 min. Brightfield images are shown to confirm presence of internalized beads. Bars = 3 µm.